

UNIVERSIDADE TÉCNICA DO ATLÂNTICO
INSTITUTO DE ENGENHARIA E CIÊNCIAS DO MAR

**WEST AFRICAN SCIENCE SERVICE CENTRE ON CLIMATE CHANGE
AND ADAPTED LAND USE**

Master Thesis

**SEASONAL VARIATION AND SOURCES OF
PARTICULATE MATTER INDUCED AIR TO SEA
NUTRIENT FLUXES IN THE EASTERN TROPICAL
NORTH ATLANTIC**

DANIEL TETTEH QUAYE

Master Research Program on Climate Change and Marine Sciences

São Vicente
2022



São Vicente
2022

UNIVERSIDADE TÉCNICA DO ATLÂNTICO
INSTITUTO DE ENGENHARIA E CIÊNCIAS DO MAR
WEST AFRICAN SCIENCE SERVICE CENTRE ON CLIMATE CHANGE
AND ADAPTED LAND USE

Master Thesis

**SEASONAL VARIATION AND SOURCES OF
PARTICULATE MATTER INDUCED AIR TO SEA
NUTRIENT FLUXES IN THE EASTERN TROPICAL
NORTH ATLANTIC**

DANIEL TETTEH QUAYE

Master Research Program on Climate Change and Marine Sciences

Supervisor | Dr. Kanneh Wadinga Fomba

São Vicente
2022

UNIVERSIDADE TÉCNICA DO ATLÂNTICO
INSTITUTO DE ENGENHARIA E CIÊNCIAS DO MAR
WEST AFRICAN SCIENCE SERVICE CENTRE ON CLIMATE CHANGE
AND ADAPTED LAND USE

**Seasonal variation and sources of particulate matter induced air to sea nutrient fluxes in
the eastern tropical North Atlantic**

Daniel Tetteh Quaye

Master's thesis presented to obtain the master's degree in Climate Change and Marine Sciences, by the Institute of Engineering and Marine Sciences, Atlantic Technical University in the framework of the West African Science Service Centre on Climate Change and Adapted Land Use

Supervisor

Dr. Kanneh Wadinga Fomba
Leibniz Institute for Tropospheric Research
(TROPOS)

São Vicente
2022

UNIVERSIDADE TÉCNICA DO ATLÂNTICO
INSTITUTO DE ENGENHARIA E CIÊNCIAS DO MAR
WEST AFRICAN SCIENCE SERVICE CENTRE ON CLIMATE CHANGE
AND ADAPTED LAND USE

**Seasonal variation and sources of particulate matter induced air to sea nutrient fluxes in
the eastern tropical North Atlantic**

Daniel Tetteh Quaye

Panel defence

President

Examiner 1

Examiner 2

São Vicente
2022



SPONSORED BY THE



Federal Ministry
of Education
and Research

Financial support

Funding for this work was provided by the German Federal Ministry of Education and Research (BMBF) within the framework of the West African Science Service Centre on Climate Change and Adapted Land Use (WASCAL) through the WASCAL Graduate Studies Programme in Climate Change and Marine Sciences at the Institute for Engineering and Marine Sciences, Atlantic Technical University, Cabo Verde.

Dedication

This thesis is dedicated to my dear family. You are my everything and I can never forget your love for me.

Acknowledgements

First, I am grateful to the Almighty God for helping me complete this chapter of my life successfully.

I am deeply thankful to my supervisor, Dr. Khanneh Wadinga Fomba, for his time, availability, mentorship, support, and constructive criticism during the completion of this thesis. His guidance taught me valuable lessons and exposed me to numerous opportunities.

I extend my appreciation to all the staff of WASCAL Cabo Verde for their assistance, especially to our caring and hardworking director, Dr. Corrine Almeida. I also want to express my gratitude to my colleagues in the WASCAL program for the memorable time we shared.

I sincerely thank Prof. Hartmut Herrmann for permitting my research internship at the Leibniz Institute for Tropospheric Research, and for providing me with access to their facilities and resources. Without the assistance of Kabore Nongma, Dr. Lekan Faboya, and Eduardo José dos Santos Souza, I would not have been able to analyse all my samples. Additionally, I want to thank Nabil Deabji for taking time to help me understand how to compute back-trajectories. I am also grateful to Dr. Holger Baars, who worked with my supervisor to help me find accommodation during my research internship.

I am immensely grateful to my family, particularly my sister, Rita Quaye, for her unwavering encouragement and prayers throughout my studies.

Finally, I appreciate all those who contributed in one way or another to my successful graduation but are not mentioned above.

Resumo

A entrada de nutrientes atmosféricos no oceano aberto é uma fonte significativa de nutrientes que afeta a produtividade biológica e a biogeoquímica marinha. Neste estudo, uma série temporal de 3 anos (2017 – 2019) de amostras de aerossóis coletadas em um local oceânico remoto no leste do Atlântico Norte tropical (ETNA) foi usada para investigar as fontes e a variação sazonal de matéria particulada (PM_{10}) derivada de nutrientes nesta região. As amostras foram analisadas para nutrientes principais solúveis (NO_3^- , NH_4^+ , and PO_4^{3-}) e metais traços totais (Al, Fe, Mn, V, Ni, Zn e Cu). A massa média de PM_{10} no local foi de $51,8 \pm 57,6 \mu g m^{-3}$, com partículas transportadas por massas de ar de quatro regiões de origem distintas com base na análise de trajetória de volta. Durante o período de amostragem, a maioria das massas de ar teve origem na Europa (55,8%) e na região do Sahel-Sahara (26,5%). Os nutrientes depositados no ETNA foram derivados de emissões naturais e antropogênicas, sendo que algumas das fontes apresentaram forte variabilidade sazonal. A poeira dominou a contribuição para os fluxos de elementos de origem crustal Al, Mn e Fe. A poeira mineral também foi a principal contribuinte para o P; no entanto, em linha com estudos anteriores, as emissões das regiões de origem descritas indicam que a queima de biomassa contribui com uma fração solúvel de P maior do que a poeira. Dos fluxos estimados de nutrientes, apenas o fluxo sazonal de NO_3^- apresentou fraca variação. A relação N:P em PM foi maior (variando de 60 a 486) do que a relação de Redfield de 16, indicando que a deposição atmosférica estava constantemente deficiente em P em relação aos requisitos de fitoplâncton. Portanto, é provável que os fluxos de nutrientes atmosféricos promovam a limitação de P no oceano ETNA oligotrófico. Como resultado, o fitoplâncton adaptado ao estresse de P será favorecido, potencialmente desencadeando um efeito cascata que afeta a estrutura da comunidade planctônica e os ciclos biogeoquímicos de N e C.

Palavras-chave: Nutrientes atmosféricos, Matéria particulada, Fluxos de nutrientes, Variabilidade sazonal, Leste do Atlântico Norte tropical, Poeira mineral.

Abstract

Atmospheric nutrient input to the open ocean is a significant nutrient source that affects biological productivity and marine biogeochemistry. In this study, a 3-year time series (2017 – 2019) of aerosol samples collected at a remote ocean site in the eastern tropical North Atlantic (ETNA) was used to investigate the sources and seasonal variation of particulate matter (PM₁₀) derived nutrient inputs to this region. The samples were analysed for soluble major nutrients (NO₃⁻, NH₄⁺, and PO₄³⁻) and total trace metals (Al, Fe, Mn, V, Ni, Zn and Cu). The average PM₁₀ mass at the site was $51.8 \pm 57.6 \mu\text{g m}^{-3}$, with particles transported by air masses from four distinct source regions based on back trajectory analysis. During the sampling period, most of the air masses originated in Europe (55.8%) and the Sahel-Sahara region (26.5%). The nutrients deposited into the ETNA were derived from both natural and anthropogenic emissions, with some of the sources exhibiting strong seasonal variability. Dust dominated the contribution to the fluxes of crustally derived elements Al, Mn, and Fe. Mineral dust was also the primary contributor of P; however, in line with previous studies, emissions from the described source regions indicate that biomass burning contributes a larger soluble fraction of P than dust. From the estimated nutrient fluxes, only the seasonal flux of NO₃⁻ showed weak variation. The N to P ratio in PM was higher (ranging from 60 to 486) than the Redfield ratio of 16, indicating that atmospheric deposition was constantly P-deficient relative to phytoplankton requirements. Therefore, atmospheric nutrient fluxes are likely to promote P-limitation in the oligotrophic ETNA ocean. As a result, phytoplankton adapted to P stress will be favoured, potentially triggering a cascade effect that impacts plankton community structure and the biogeochemical cycles of N and C.

Keywords: Atmospheric nutrients, Particulate matter, Nutrient fluxes, Seasonal variability, Eastern tropical North Atlantic, Mineral dust.

Abbreviations and acronyms

ACE	Atlantic Coastal Europe
ARL	Air Resource Laboratory
ATM	Atlantic Marine
CAA	Coastal Africa and Atlantic
CCN	Cloud condensation nuclei
CVAO	Cape Verde Atmospheric Observatory
EC	Elemental carbon
ETNA	Eastern Tropical North Atlantic
EUSAAR	European Supersites for Atmospheric Aerosol Research
FTP	File transfer protocol
GDAS	Global Data Assimilation System
HPLC	High Performance Liquid Chromatography
HV	High volume
HYSPLIT	Hybrid Single-Particle Lagrangian Integrated Trajectory
IC	Ion Chromatography
ICP	Inductively Coupled Plasma
IN	Ice Nuclei
NCAS	National Centre for Atmospheric Science
NOAA	National Oceanic and Atmospheric Administration
nss-K⁺	Non-sea salt potassium
PM	Particulate matter
PM₁₀	Particulate matter with aerodynamic diameter less than 10 µm
RFIC-EG	Reagent-Free Ion Chromatography-Eluent Generation
SAL	Saharan Air Layer
SSA	Sahel-Sahara Africa
SST	Sea surface temperature
TROPOS	Leibniz Institute for Tropospheric Research
TXRF	Total reflection X-ray fluorescence

General index

Financial support	i
Dedication	ii
Acknowledgements	iii
Resumo	iv
Abstract	v
Abbreviations and acronyms	vi
General index	vii
Figure index.....	ix
Table index.....	xi
1. Introduction	1
1.1 Background and context.....	1
1.2 Problem statement	2
1.3 Research questions	3
1.4 Relevance and importance of the research.....	3
1.5 Objectives of the work	3
1.6 Structure of the work.....	4
2. Literature review	5
2.1 Particulate matter (aerosol particles).....	5
2.2 Sources, types and composition of particulate matter.....	5
2.3 Importance of particulate matter	6
2.3.1 Climate	6
2.3.2 Air quality	6
2.3.3 Ocean ecosystems	7
3. Materials and Methods	10
3.1 Sampling site.....	10
3.2 Meteorological conditions at the sampling site.....	10
3.3 Sample collection	11
3.4 Particulate matter mass concentration.....	12
3.5 Trace metal analysis	12
3.5.1 Carrier cleaning	12
3.5.2 Internal standard preparation.....	13
3.5.3 Sample digestion	13
3.5.4 Sample preparation.....	14
3.5.5 Analytical technique.....	14
3.5.6 Measurement instrument	15

3.5.7	Sample measurement.....	16
3.6	Ion analysis.....	16
3.6.1	Sample preparation.....	16
3.6.2	Analytical method and sample measurement.....	16
3.6.3	Measurement instrument.....	18
3.7	Elemental carbon analysis.....	18
3.8	Data analysis.....	18
3.8.1	Calculation of atmospheric concentrations.....	18
3.8.2	Determination of PM ₁₀ source regions.....	19
3.8.3	Estimation of dust.....	20
3.8.4	Estimation of non-sea salt potassium.....	20
3.8.5	Calculation of nutrient deposition fluxes.....	20
4.	Results and Discussion.....	22
4.1	Chemical composition of PM ₁₀	22
4.2	Mass concentration of PM ₁₀	23
4.2.1	Temporal variation.....	23
4.2.2	Seasonal variation.....	24
4.3	Air masses.....	26
4.3.1	Cluster analysis.....	26
4.3.2	Seasonal changes in air mass origin.....	27
4.4	Nutrient sources.....	29
4.4.1	Contribution of source regions.....	29
4.4.2	Species interrelationship.....	30
4.4.3	Source markers.....	31
4.5	Nutrient deposition.....	34
4.5.1	Temporal variation.....	34
4.5.2	Seasonal variation.....	37
4.6	Redfield ratio.....	41
4.7	Implications of the study.....	42
5.	Conclusions.....	44
6.	References.....	45
	Appendix A. Statistical summary of the mass concentration of particulate matter (PM ₁₀), water soluble ions and trace metals analysed in the aerosol samples.....	56

Figure index

Figure 1. Map of the Cape Verde Islands (delimited by the red rectangle) in the eastern tropical North Atlantic (A) and the location of the sampling site on São Vicente marked by the red symbol (B). The high-volume sampler used for sampling (C) and the Cape Verde Atmospheric Observatory (D).....	11
Figure 2. Schematic of total reflection X-ray fluorescence (TXRF) analysis. A) Production of X-ray fluorescence radiation. B) Basic TXRF instrument setup. C) Exemplary spectrum of a multi-element sample from a TXRF analysis. D) The S4 T-STAR spectrometer used for trace metal analysis.	15
Figure 3. Schematic of the setup of an ion chromatograph (Source: Chagué-Goff & Wong, 2013).....	17
Figure 4. Ion chromatography (IC). An example of a chromatogram displayed on the monitor of a computer during analysis (A). The Dionex IC system used for ion analysis and its accessories (B).....	17
Figure 5. Annual variability of PM ₁₀ mass concentration during the study period.....	24
Figure 6. Boxplots of the monthly particulate matter (PM ₁₀) mass concentration for the three years (2017, 2018, and 2019). Boxes show interquartile range and the horizontal bar in each box shows the median. Upper and lower limits of the whiskers represent the 90th and 10th percentiles of the data. Black dots are the extremes (values greater or less than 1.5 times the interquartile range above or below the upper and lower quartiles, respectively).	25
Figure 7. Distinct air mass clusters (4) obtained from the clustering of all 96-hr backward trajectories ending at the Cape Verde Atmospheric Observatory (CVAO) during the study period. The percentages shown represent the proportion of total trajectories in each cluster.	26
Figure 8. Typical 96-hr back trajectories at 6-hr intervals representative of the identified air mass categories Sahel-Sahara Africa — SSA (top-left), Atlantic Coastal Europe — ACE (top-right), Atlantic Marine — ATM (bottom-left) and Coastal Africa and Atlantic — CAA (bottom-right).....	27
Figure 9. Seasonal changes in the air mass clusters (Cluster 1 — C1, Cluster 2 — C2, Cluster 3 — C3 and Cluster 4 — C4) influencing the Cape Verde Atmospheric Observatory over the sampling period.	28
Figure 10. Relative contribution of the four identified source regions (Sahel-Sahara Africa (C1), Atlantic Coastal Europe (C2), Atlantic Marine (C3) and Coastal Africa and Atlantic (C4)) to concentrations of nutrient species observed at the Cape Verde Atmospheric Observatory over the study period.	29
Figure 11. Correlation coefficients of nutrient species, non-sea salt potassium (nss_K), and dust component of aerosol particles collected at the Cape Verde Atmospheric Observatory. Correlations are significant at the 0.05 level (pairwise) in all boxes except those marked with a red cross.....	30
Figure 12. Time series of elemental carbon (EC) and non-sea salt potassium (nss_K) measured during the study period.....	31
Figure 13. Monthly mean non-sea salt potassium (nss-K ⁺) to potassium (K ⁺) ratio (denoted as inverted triangles) and nss-K ⁺ concentration (denoted as bars).....	32

Figure 14. Boxplots of monthly V to Ni ratio. Red dots represent the mean, and the dashed blue line is the minimum threshold ratio (0.7) that signals the influence of ship emission.....	32
Figure 15. Temporal variation of the nutrient deposition flux of total Al, Fe and Mn.	35
Figure 16. Temporal variation of the nutrient deposition flux of total Cu and Zn.....	35
Figure 17. Temporal variation of the nutrient deposition flux of total V.....	36
Figure 18. Temporal variation of the nutrient deposition flux of soluble NO_3^- , NH_4^+ and PO_4^{3-}	36
Figure 19. Boxplots of monthly deposition fluxes of total Ni and V. Black and non-black dots represent the mean and extreme values, respectively.	37
Figure 20. Boxplots of monthly deposition fluxes of total Al, Fe and Mn.	38
Figure 21. Boxplots of monthly deposition fluxes of total Cu and Zn.....	38
Figure 22. Boxplots of monthly deposition fluxes of NO_3^- , NH_4^+ and PO_4^{3-}	40
Figure 23. Monthly mean molar N:P ratio in aerosol samples.....	41

Table index

Table 1. Summary of filter samples collected at the Cape Verde Atmospheric Observatory (CVAO) from 2017 – 2019 and used in this work.	12
Table 2. Statistical summary of the mass concentration of particulate matter (PM ₁₀), select water-soluble ions and trace metals from the list of chemical components analysed in aerosol samples collected over the study period (2017 - 2019). Aerosols sampled in 2019 were not considered in obtaining trace metal values.	22
Table 3. Mean (\pm standard deviation) and range (in parentheses) of seasonal flux of total bioactive trace metals and soluble major nutrients.	39

1. Introduction

1.1 Background and context

Atmospheric deposition of particulate matter (aerosol particles) is recognised as an important source of nutrients and trace metals in marine ecosystems (Baker & Jickells, 2017; Duce et al., 2009; Kanakidou et al., 2018; Mahowald et al., 2017; Seok et al., 2021). Inputs of macronutrients (nitrogen (N) and phosphorous (P)) and micronutrients (including iron (Fe), zinc (Zn), cobalt (Co), manganese (Mn), vanadium (V), nickel (Ni), copper (Cu), and cadmium (Cd); Sunda, 2012) from atmospheric deposition have been shown to affect nutrient stoichiometry, phytoplankton growth, nitrogen fixation, carbon export and microbial community composition (Guo et al., 2022). All-inclusively, these impacts work in the long term to alter ocean biogeochemistry (direct effect) and influence the Earth's climate (indirect effect) by stimulating carbon dioxide (CO₂) removal from the atmosphere via the biological pump (Mahowald et al., 2017; Seok et al., 2021). Once emitted into the atmosphere, nutrient-bearing particulate matter (PM) can be carried over long distances and deposited in the open ocean (Ventura et al., 2021). During transport, the particle size, composition, and atmospheric processing determine the solubility of PM nutrient species. This solubility dictates the bioavailability of nutrients in the ecosystem into which PM is deposited (Chien et al., 2016).

The eastern tropical North Atlantic (ETNA) Ocean is of particular scientific interest as an oligotrophic region (Kiko et al., 2020) that receives a significant input of PM annually. The area is close to the Sahel and Sahara desert regions of North Africa, which are major sources of mineral dust (Gong et al., 2020; Kumar et al., 2018). The dust load from the Saharan Desert into the North Atlantic constitutes the largest deposition to the world's oceans, accounting for 100 – 220 Tg yearly. Saharan dust also co-transported anthropogenic aerosols into the ETNA (Powell et al., 2015). Dust events can contain high amounts of nutrients and trace elements. Such extreme weather phenomena also show strong temporal variability (Mahowald et al., 2018; Fomba et al., 2014).

Long-term aerosol deposition research in the ETNA has been consigned to sampling on research cruises passing through the region (Baker et al., 2010, 2013; Powell et al., 2015) and as part of major survey programs (GEOTRACES and the Atlantic Meridional Transect) over the Atlantic (Baker & Jickells, 2017; Jickells et al., 2016). Measurements from Island sites, such as the Cape Verde Atmospheric Observatory (CVAO), unlike those from these research

cruises, provide greater resolution over extended temporal scales and are accompanied by comparatively higher sample numbers. Therefore, these sites facilitate easy estimation of seasonal variations and annual deposition fluxes (Powell et al., 2015). Anderson et al. (2016) reported that it is challenging to derive deposition fluxes for remote ocean areas. In addition, Fomba et al. (2014) found that relatively little is known about long-term observations from remote ocean sites in the ETNA.

The Cape Verde Islands are well situated for conducting studies on PM deposition to the ETNA. The islands are positioned in the domain of mineral dust transport over the tropical North Atlantic (Patey et al., 2015) and are also subjected to atmospheric conditions comparable to those of the ETNA (Fomba et al., 2013). The CVAO, similar to other island sites in the North Atlantic, for example: Santa Cruz de Tenerife (Castillo et al., 2017), Mace Head (O'Dowd et al., 2013), Bermuda, and Barbados (López-García et al., 2021); facilitates the collection of long-term in-situ data for estimating particle concentration, chemical composition, and deposition fluxes (Powell et al., 2015). Unfortunately, it is difficult to retrieve this information from satellite observations (Patey et al., 2015). Therefore, to contribute to current advances, long-term observations at the CVAO can be used to retrieve the information needed to validate atmospheric transport models, which are used to estimate particle-induced air to sea nutrient fluxes and predict future changes (Powell et al., 2015).

1.2 Problem statement

Particulate matter (PM) can carry nutrients that are transported atmospherically to open ocean areas beyond the reach of fluvial input. Once deposited, they influence nutrient availability, biological productivity, and air-sea CO₂/O₂ exchange (Chien et al., 2016). Owing to the diversity of sources and transport mechanisms, PM availability varies in space and time, with any particular region subject to potential inputs from several sources.

Over the Cape Verde archipelago, situated in the oligotrophic ETNA ocean, mineral dust deposition serves as a major source of PM. Deposition peaks in winter when dust transport takes place in low-altitude air layers and subsides to its lowest in summer when transport occurs in high-altitude air layers conveying dust to the western North Atlantic (Carpenter et al., 2010; Kumar et al., 2018). This seasonal variability possibly impacts PM nutrient supply and, hence, nutrient stoichiometry along with patterns of (co-)limitation.

Additionally, assessing the sources of nutrients in PM and their fluxes is critical, especially due to the rise in anthropogenic activities and the predicted increase in regional dust emissions (Mahowald et al., 2018).

Therefore, this study aimed to assess the sources and seasonal variation of particle nutrient fluxes to the ETNA using long-term continuously collected PM samples.

1.3 Research questions

- What is the PM nutrient budget in the region of the ETNA?
- What are the sources of atmospheric derived nutrients to the ETNA?
- How does the atmospheric flux of nutrients to the ETNA vary seasonally?

1.4 Relevance and importance of the research

This study improves our understanding of how seasonality potentially affects the stoichiometry of nutrients deposited in ocean surface waters. According to Moore et al. (2013), having a good appreciation of the variation in the stoichiometry of nutrient input is critical for assessing the effects on phytoplankton. This is because phytoplankton have different cellular elemental ratios.

The findings of this study will also contribute to describing atmospheric nutrient inputs to the tropical North Atlantic, as quantifying nutrient fluxes is crucial for estimating their impact. In addition, information on PM nutrient composition is valuable for modellers seeking to constrain atmospheric nutrient fluxes to the region or better represent external nutrient inputs in biogeochemical models.

In the face of ongoing human-induced changes, it is vital to differentiate between anthropogenic and natural sources of PM nutrient inputs. This will provide insight into how changes in atmospheric chemical composition may influence nutrient cycling in the ocean ecosystem (Desboeufs et al., 2018).

1.5 Objectives of the work

This study aimed to investigate the abundance of atmospheric particle nutrient fluxes in the ETNA region and to determine the following:

- their source regions by applying different trajectory models and source signatures.

- their temporal and seasonal trends.

1.6 Structure of the work

This work is organised into six major chapters. The context and motivation for the study are presented in Chapter 1, and the relevant literature is discussed in Chapter 2. Chapter 3 describes the methods used to address the research questions. The results of various analyses applied to the data are detailed in Chapter 4, followed by a discussion of the findings in Chapter 5. Finally, the main conclusions drawn from this study are presented in Chapter 6.

2. Literature review

2.1 Particulate matter (aerosol particles)

Aerosol particles are ubiquitous over the Earth's surface. Reviews by Kanakidou et al. (2018), Prather et al. (2008), and a report by Mahowald (2011) have all described aerosol particles as suspended solids found in the atmosphere. These particles can be too small to be observed by the naked eye or sufficiently large to be seen. Their sizes range from 1 nm to about 100 μm according to Mahowald et al. (2011). Kanakidou et al. (2018) also expresses a similar size range but with a lower limit of 3 nm instead. In general, particle size in terms of diameter, can be said to vary from a few nanometres to tens of micrometres (Tomasi & Lupi, 2016). Based on the size range, particles may be classified as either fine (diameter $<1 \mu\text{m}$) or coarse (diameter $>1 \mu\text{m}$) PM (Mahowald et al., 2011). Additionally, the most common PM size fractions are $\text{PM}_{2.5}$ and PM_{10} , which are, PM with aerodynamic diameter below 2.5 μm and 10 μm , respectively (Ventura et al., 2021).

2.2 Sources, types and composition of particulate matter

Particulate matter is a key component of the atmosphere. Depending on whether a particle is emitted or formed, it can be classified as either a primary or secondary aerosol particle. Primary aerosols include particulates such as sea salt, mineral dust, volcanic ash, soot, pollen, and smoke, which are directly released into the atmosphere (Kolb & Worsnop, 2012). In contrast, secondary aerosols are particulates formed through the condensation of a gas or a chemical reaction (Mahowald et al., 2011). However, when PM grows through condensation to become a cloud droplet, it is no longer considered an aerosol particle. Likewise, precipitation forms such as rain drops and ice crystals, are not considered aerosol particles (Tomasi & Lupi, 2016).

The sources of PM are diverse. Both natural and anthropogenic processes result in the release of PM into the atmosphere. Natural sources include wind-borne dust, sea spray emissions, wildfires, biogenic particles, and volcanic eruptions (Hamilton et al., 2022). Anthropogenic sources include fuel and coal combustion, industrial activities such as agriculture and mining, vehicular emissions, and biomass burning (Klimont et al., 2017; Kumari et al., 2021). This wide range of sources, coupled with the different transformation pathways particulates undergo during atmospheric transport, determines the chemical constituents of aerosol particles (Tomasi & Lupi, 2016).

Therefore, the chemical components of PM are highly variable, with components either inside or on the particle's surface (Kelly & Fussell, 2012). Constituents of PM include ionic species such as NO_3^- , PO_4^{3-} , NH_4^+ , SO_4^{2-} , NO_2^- , Br^- , F^- , Cl^- , Na^+ , and Mg^{2+} (Mateus-Fontecha et al., 2022); carbonaceous species (Fomba et al., 2014); metals including Al, K, Ca, Ti, Cr, Fe, Co, Cu, Cd, V, Ni, Se, Sr, Zn, Mn, Mo, Ag, Sb, Pb, and Bi (Fomba et al., 2020); metalloids (Si and As); and organics (Deabji et al., 2021; Mateus-Fontecha et al., 2022).

2.3 Importance of particulate matter

Particulate matter naturally constitutes a part of the Earth system. Over the few last decades, their concentration and variety in the atmosphere have increased due to urbanisation and industrialisation (Rodríguez & López-Darias, 2021). These particles have direct and indirect effects on major reservoirs of the Earth, and consequently, our lives. Furthermore, more people have become conscious of the health effects of PM (Chen et al., 2020). As a result, there has been growing scientific interest in PM. The effects of PM on climate, air quality, and ocean ecosystems are discussed below.

2.3.1 Climate

The Earth's climate is influenced by PM via several pathways. The direct climate forcing of PM involves scattering and absorption of solar radiation (Ghan et al., 2012; Qian et al., 2011). Whether scattering or absorption occurs depends on the particle's composition (Sudheer & Rengarajan, 2012). Indirectly, aerosols modify cloud microphysics (Qian et al., 2011), optical properties (Mahowald et al., 2017), cloud cover, and precipitation patterns by functioning as cloud condensation nuclei — CCN (van Pinxteren et al., 2020) and ice nuclei — IN (Mahowald et al., 2011; Ventura et al., 2021). In addition, Rodríguez and López-Darias (2021) and Ghan et al. (2012), indicate another category known as the semi-indirect effect. This describes climate feedback linked to cloud response to warming by aerosols such as soot. Therefore, aerosol particles are critical determinants of climate at the regional and global scales. Their net effect on Earth's climate system is cooling (Kaufman et al., 2002).

2.3.2 Air quality

Particulate matter contributes heavily to air pollution. Air pollution reduces visibility (Ayanlade et al., 2019) and negatively affects transportation (Zhong et al., 2020). Polluted air can also affect human health. Inhalation of PM, particularly fine particles, has been linked to increased

respiratory and cardiovascular diseases (Chen et al., 2020; Zhong et al., 2020). Such health effects result from both short- and long-term exposure. The World Health Organization Regional Office for Europe (2013) attributed PM to 5% of lung cancer related deaths and 3% of cardiopulmonary deaths worldwide. Hence, it is necessary to regulate the occurrence of PM in the air. To achieve this, limits on the concentrations of PM₁₀ and PM_{2.5} are used as proxies for assessing air quality.

2.3.3 Ocean ecosystems

Particulate matter can be transported over long distances through the atmosphere and deposited in marine ecosystems (Mahowald et al., 2017). As previously mentioned, PM is composed of numerous chemical species. Some of these species are essential nutrients for ocean ecosystems (Guo et al., 2022). Particulate matter reaches ocean surface waters through either wet scavenging (rain washout) or dry deposition. Before deposition, the atmospheric chemical processing of the particles largely dictates the bioavailability of the nutrient species (Guo et al., 2022; Kaushik et al., 2021). Both macro- and micronutrients are supplied by PM. Macronutrients include phosphorus and nitrogen species PO₄³⁻, NO₃⁻, and NH₄⁺ (Ventura et al., 2021), while micronutrients include Fe, Co, Cu, Cd, V, Ni, Zn, Mn and Mo. Atmospheric deposition of nutrient-laden aerosol particles is thus a key source of nutrients to the ocean (Sunda, 2012). In the ocean, dissolved nutrients from deposited particles can affect nutrient stoichiometry, N₂ fixation, biogeochemical cycles, inhibit phytoplankton growth, and change microbial community composition (Guo et al., 2022).

- ***Change in nutrient stoichiometry***

Nutrient availability is a key determinant of marine biological productivity, with N and P being the main limiting nutrients (Krishnamurthy et al., 2010). Moore et al. (2013) recognizes that for optimum phytoplankton production, these two nutrients should exist in the ratio 16:1 (N:P) — the Redfield ratio. For example, the addition of reactive inorganic N species from aerosol particles has proven effective in increasing phytoplankton biomass, particularly in oligotrophic waters (Guo et al., 2022). It has also been observed that the amount of N supplied by atmospheric deposition is consistently higher than that of P (Okin et al., 2011). Consequently, the supply of N by PM deposition in excess of the required P may cause an imbalance in the Redfield ratio, leading to P limitation in oligotrophic environments.

- ***Nitrogen fixation and biogeochemical cycles***

Iron (Fe) is a vital micronutrient that regulates primary production in most oceans worldwide (Trapp et al., 2010). It co(-limits) the N₂ fixation capacity of nitrogen-fixing microorganisms and impacts carbon sequestration (Myriokefalitakis et al., 2018). The growth and activity of these microorganisms are also limited by low P concentrations (Mahowald et al., 2018). Aerosol deposition adds critical nutrients, including N, P, Fe and Si to the ocean, which alter nitrogen and carbon cycles (Krishnamurthy et al., 2010). In a recent study by Zhou et al. (2021), Al was proposed to promote phytoplankton growth, nitrogen fixation, and carbon export, as well as influence the removal of CO₂ from the atmosphere.

- ***Inhibition effect and shift in community composition***

The deposition of trace metal bearing PM has been reported to inhibit phytoplankton growth and modify community composition (Guo et al., 2022). Mahowald et al. (2018) carried out a review into the effect dissolving trace metals from deposited PM had on marine microorganisms. The authors express that albeit micronutrients like Zn, Mn, Co do not exert the same level of control over primary production as Fe, they still play a crucial role in marine biogeochemistry by modifying microbial community composition. They achieve this by serving as structural factors in microbial cells and controlling the enzymes that these cells can express. Zinc and Co function as co-factors in carbonic anhydrase, a carbon-fixing enzyme (Baker et al., 2007). In addition, in alkaline phosphatase, Fe and Zn are utilised as co-factors (Mahowald et al., 2018). Conversely, Cu, although needed in trace amounts for growth, becomes toxic at high concentrations. This observation was confirmed by Jordi et al. (2012) and Paytan et al., (2009), who demonstrated the negative effects of elevated Cu concentrations on phytoplankton in the western Mediterranean Sea and the Bay of Bengal, respectively. Both studies found that Cu-rich PM deposition led to a reduction in the phytoplankton biomass. The potential to alter phytoplankton community structure is also indicated. Moreover, Pinedo-González et al. (2015) acknowledged Ni and V as bio-essential elements that act as co-factors in the enzymes hydrogenase and nitrogenase, respectively, and may restrict phytoplankton production. Nickel also functions as the active metal centre in urease, which plays a role in the absorption of urea as a source of N.

- *Ballasting effect*

In addition to the impacts of bioavailable nutrients, insoluble particles also affect the marine ecosystem. Van der Jagt et al. (2018) studied the ballasting influence of PM, specifically Sahara dust, on ocean carbon export off Cape Blanc — Mauritania. They found that the integration of dust particles into aggregated organic material serves as ballast, which enhances aggregate sinking speeds and likely elevates ocean carbon export. Notwithstanding, they observed that the mineral dust did not scavenge suspended particles while sinking through the water column. Overall, the study revealed a ten-fold increase in carbon export when mineral dust was responsible for ballasting the aggregate.

In conclusion, the various impacts discussed above highlight the importance of understanding atmospheric nutrient fluxes and their variability. It is crucial to note, however, that these impacts are not universal. Mahowald et al. (2018) emphasise that the impacts of atmospheric nutrient deposition may vary depending on factors such as the ocean region experiencing the deposition, the mode of deposition, the nutrient composition, and the biota present in the ecosystem. Therefore, a region-specific approach is required to understand the diverse effects of atmospheric nutrient flux.

3. Materials and Methods

3.1 Sampling site

Samples of PM₁₀ were collected at the Cape Verde Atmospheric Observatory (16° 51.490 N, 24° 52.020 W), situated in the eastern part of São Vicente, Cape Verde (Fig. 1-A). São Vicente forms part of the 10 Cape Verde archipelago islands located in the ETNA (Fig. 1-B). Conditions on the island are arid and semi-arid, dry and hot (Freire et al., 2020), with scarce rainfall, a yearly average air temperature of 23.6 °C and mean relative humidity of 79 % (van Pinxteren et al., 2020). Thus, wet particle deposition in the area is unimportant. The site is 800 km from the West African coast (Kumar et al., 2018), 70 m from the shoreline and 10 m a.s.l. Due to its location, the site mostly experiences north-easterly trade winds and negligible influence from local anthropogenic emissions (Fomba et al., 2014). The CVAO (Fig. 1-C) thus serves as an ideal site for continuous monitoring of long-range PM transport into the ETNA. Hence, data collected at the station can be considered representative of the atmosphere over the surrounding open ocean.

3.2 Meteorological conditions at the sampling site

Data on the meteorological parameters (relative humidity, temperature, wind speed and direction) at the CVAO were obtained from the National Centre for Atmospheric Science (NCAS) – England. This data was collected on top of the 30m tower at the CVAO with a Vantage Vue automatic weather station (Davis Instrument, England) at a rate of 2.5 s.

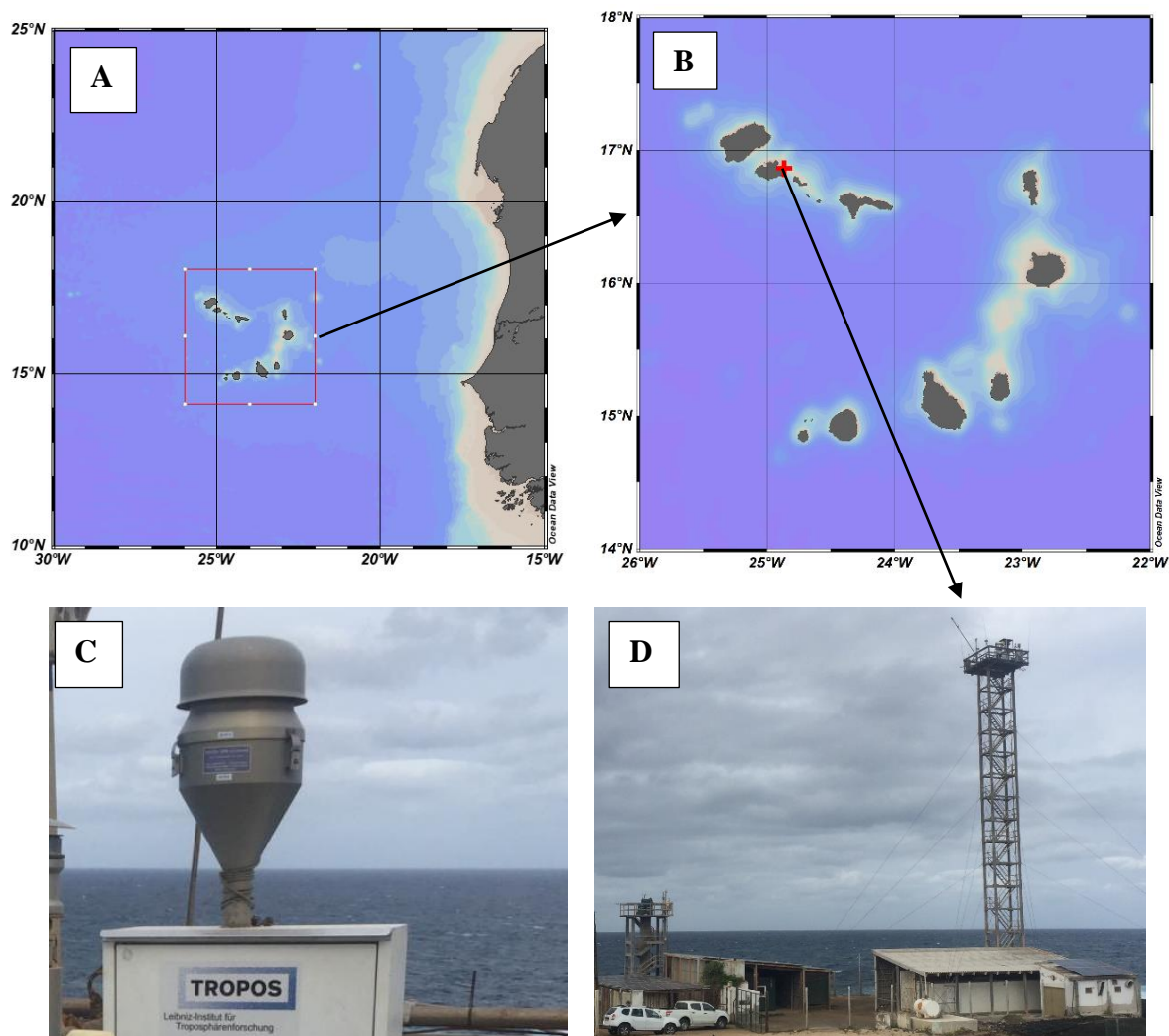


Figure 1. Map of the Cabo Verde Islands (delimited by the red rectangle) in the eastern tropical North Atlantic (A) and the location of the sampling site on São Vicente marked by the red symbol (B). The high-volume sampler used for sampling (C) and the Cape Verde Atmospheric Observatory (D).

3.3 Sample collection

The sampling of PM_{10} was carried out at the top of a 30 m measurement tower at CVAO. This was to limit the impact of sea spray on the sampled particles. Sampling was done using a high volume (HV) PM_{10} Digital (DHA-80, Walter Riemer Messtechnik, Germany) collector (Fig. 1-A). This was operated at a mean flow rate of $30.0 \text{ m}^3/\text{hr}$. The samples were collected on quartz fibre filters (Munktell, MK 360) over a 72-hr period except during rigorous campaigns when this was adjusted to 24 hrs. Field blank filters were also collected: filters deployed in the field but without the sampler sucking air through. Unfortunately, this sampling routine was not always achieved due to power outages and instrument downtime. These two factors further caused sampling in December 2019 to abruptly end on the 17th instead of the 31st. The sampling period investigated in this study was from January 2017 to 17th December, 2019. A summary

of all filters used in this study and their particular sampling routine is presented in Table 1. After sampling, filters were frozen at $-20\text{ }^{\circ}\text{C}$ prior to being transported to Leipzig, Germany for storage until analysis. Storing filters frozen prevents samples from reducing in solubility (Patey et al., 2015).

Table 1. Summary of filter samples collected at the Cape Verde Atmospheric Observatory (CVAO) from 2017 – 2019 and used in this work.

	2017	2018	2019
Total samples	134	129	157
72 hr samples	100	113	75
24 hr samples (Intensive campaign)	28	9	66
Other samples (not 24 or 72 hrs)	6	7	16

3.4 Particulate matter mass concentration

The PM_{10} mass concentration was determined by gravimetry. Sampled filters were weighed with a microbalance (Mod. AT261 Delta Range, Mettler-Toledo) after being stabilised for three days at a constant temperature of $20 \pm 1\text{ }^{\circ}\text{C}$ and relative humidity of $50 \pm 5\%$ before and after sampling. The weight difference was calculated and divided by the total sampling volume to derive the mass concentration.

3.5 Trace metal analysis

Trace metals were measured using total reflection X-ray fluorescence (TXRF; S4 T-STAR, Bruker Nano, GmbH, Germany) technique. To measure the trace metal content of collected PM_{10} samples using TXRF, a number of procedures were completed in the laboratory. These involved; cleaning of the TXRF sample carriers, digestion of samples, preparation of samples and quantification of the trace metals. Excluding samples collected in 2019, all other samples were used in the trace metal analysis.

3.5.1 Carrier cleaning

Using clean sample carriers is essential to avoid errors during trace metal quantification and to carry out a successful TXRF analysis. Quartz glass discs (height of 3 mm, diameter of 30 mm; Bruker Nano, GmbH, Germany) were used as sample carriers for the TXRF measurements. The carriers were pre-cleaned consecutively with acetone (HPLC grade, $> 99.8\%$, CHROMASOLV, Sigma-Aldrich, Germany) and ethanol (HPLC grade, $> 99.8\%$,

CHROMASOLV, Sigma-Aldrich, Germany) using fluff-free Kimwipes and mounted on washing cassettes. After this step, the carriers were boiled in three cleaning solutions successively: 35% concentrated HCl (supra-quality, ROTIPURAN, Roth Germany), 69% concentrated HNO₃ (supra-quality, ROTIPURAN, Roth Germany), and a detergent solution (RBS 50, 4% concentrated), respectively. Each heating step was performed at 300 – 350 °C for 2 hrs on a heating plate in a fume hood. During heating, mounted carriers were consistently submerged in the beaker of solution and covered by a watch glass. In-between solutions, carriers were rinsed with ultrapure water and sonicated for 30 mins. After rinsing, the carriers were dried in an oven and allowed to cool to room temperature. They were then siliconised by applying 5 µl silicon solution in isopropanol (Merck, Germany) to the carrier surface centre. The silicon solution is to help confine applied liquid aliquots to the centre of the carrier. Finally, the TXRF was used to conduct purity control tests on the cleaned carriers to confirm their cleanliness. Sample carriers determined to be clean were then stored in clean petri dishes until usage.

3.5.2 Internal standard preparation

Internal standard solutions were prepared to facilitate trace element quantification. These were prepared using 1000 mg/l inductively coupled plasma (ICP) standard solution of cobalt (Co; Roth, Germany) and 1000 mg/l ICP standard solution of gallium (Ga; Merck, Germany). High purity 69 % concentrated HNO₃ (ROTIPURAN, Roth Germany) solution was used for dilution. An initial solution (5 ml) was prepared by mixing the 1000 mg/l Ga and Co solutions in a 1:1 ratio, and diluted to 25 ml in a volumetric flask. A 2.5 ml aliquot of this solution was further diluted in a 1:9 ratio in another volumetric flask. Afterwards, 2.5 ml of this recent solution was diluted similarly in a 1:9 ratio. Therefore, the final concentration of the three internal standards obtained were 100, 10 and 1 ng/µl.

3.5.3 Sample digestion

A ceramic puncher was used to cut out three spots of 8 mm diameter from each sample filter. Cut-out filters were transferred into 10 ml acid-cleaned Teflon bombs and digested in 1.5 ml solution of HNO₃ and HCl in the ratio 3:1. The use of reverse aqua regia (3 HNO₃ : 1 HCl) provides higher recovery as compared to other solutions (Fomba et al., 2020). The bombs were digested for 2 hrs under high-pressure conditions in a MARS 6 (CEM GmbH, Germany) microwave. Digestion washes particulates off the filter surface to produce a homogenous

solution indicative of the sample that can be readily measured. After cooling, the digested solutions were transferred into 2 ml vials.

3.5.4 Sample preparation

A 10 μ l aliquot of the digested solution was pipetted onto the centre of the previously cleaned and siliconised sample carrier. Afterwards, the solution was evaporated on a heating plate at 100 °C for about 10 min. Placing the sample at the centre of the carrier surface and ensuring it does not spread beyond a 10 mm diameter to facilitate an effective sample excitation, thereby enhancing measurement sensitivity. The multi-element (Ga + Co) internal standard earlier prepared was then added to the dried sample to aid element quantification. Depending on visually determined PM₁₀ filter loading, 10 μ l of the different standard concentrations was used: 100, 10 and 1 ng / μ l for densely loaded, moderately loaded and less loaded filters, respectively. After the spiking with internal standards, the carrier was reheated. These steps were all carried out under a laminar flow hood. Once the carrier cooled down, the sample on it was measured. Additionally, field blank filters used for blank correction were analysed following the same steps.

3.5.5 Analytical technique

Total reflection X-ray fluorescence (TXRF) technique was used to quantify trace metals in the samples. The working principle is that atoms, when illuminated with X-rays, emit secondary X-rays (fluorescence radiation) when an electron from a higher orbital falls down to replace an electron ejected from a lower orbital (Bruker Nano GmbH, 2017; Fig 2-A). In TXRF analysis, an X-ray tube produces an X-ray beam that is converted into a narrow energy band by a multi-layered monochromator. The beam hits on a polished sample carrier at an angle smaller than a certain critical incident angle and is totally reflected (Fig. 2-B).

Once elements in the sample on the carrier become excited by the incident X-ray beam, they emit fluorescence radiation at characteristic energies. This energy is detected and converted into a voltage pulse whose intensity is proportional to the energy. All pulses are later converted into a digital spectrum and assigned to specific channels. The digital spectrum, displayed through a software contains fluorescence lines of sample elements, excitation radiation and the total counts of X-ray energy per channel (Fig. 2-C). The spectrum is then subjected to spectra correction, background correction and peaks deconvolution to distinguish elements. In identifying elements, fluorescence lines in the corrected spectrum are compared with a

prestored data library of fluorescence lines for various elements. Identified elements were then quantified using an internal standard added to the sample before measurement. The concentration of each element is computed from the following equation:

$$C_i = \frac{C_{IS} \times N_i \times S_{IS}}{N_{IS} \times S_i} \quad (1)$$

Where C_i is the concentration of the element to be analysed; C_{IS} is the internal standard concentration; N_i is the net pulse number in the measured spectrum of the element to be analysed; N_{IS} is the net pulse number in the measured spectrum of the internal standard; S_i is the sensitivity factor of the element and S_{IS} is the sensitivity factor of the internal standard element.

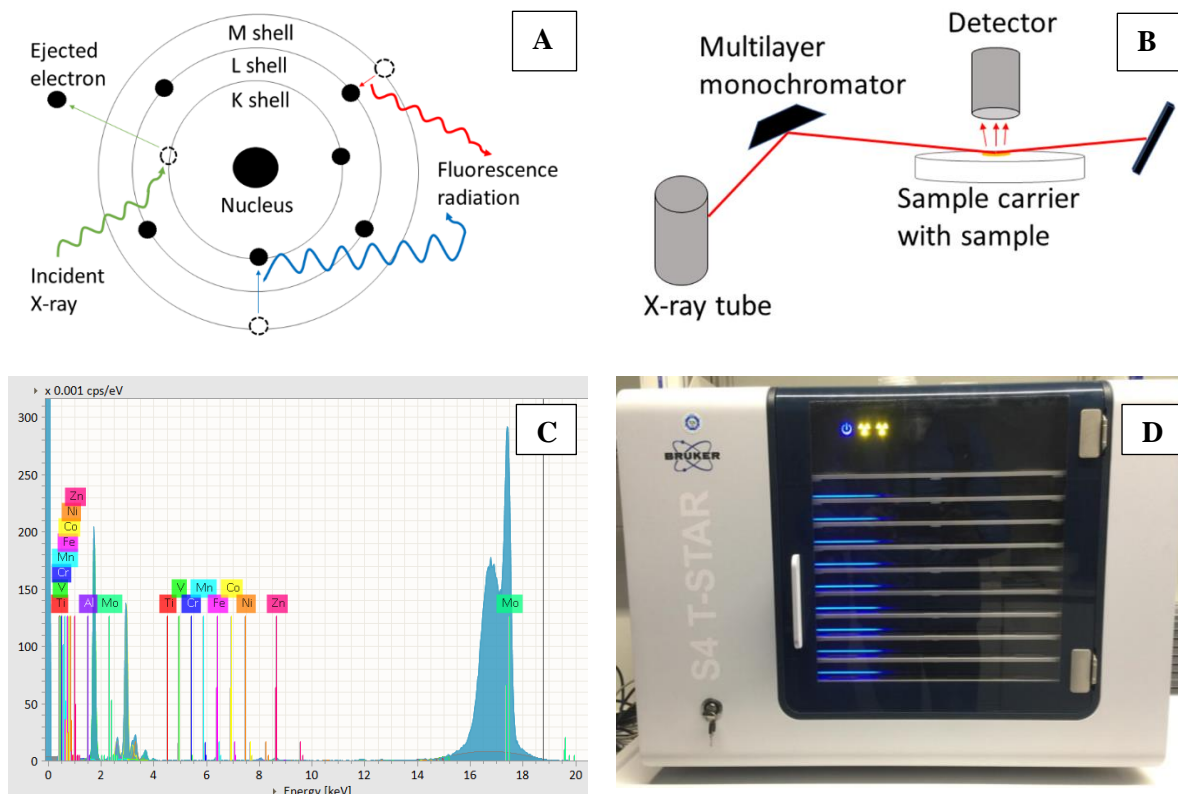


Figure 2. Schematic of total reflection X-ray fluorescence (TXRF) analysis. A) Production of X-ray fluorescence radiation. B) Basic TXRF instrument setup. C) Exemplary spectrum of a multi-element sample from a TXRF analysis. D) The S4 T-STAR spectrometer used for trace metal analysis.

3.5.6 Measurement instrument

Analysis of trace metals was achieved with a benchtop S4 T-STAR TXRF spectrometer (Fig. 2-D). This instrument is equipped with two X-Ray tubes (molybdenum, Mo and tungsten, W), a multilayer monochromator and an XFlash Si drift detector. The detector is positioned < 2 mm

from the sample carrier to reduce scattered background in the derived spectra and ensure high efficiency of the fluorescence radiation. The Mo and W tubes have excitation lines of 17.5 KeV and 8.5 KeV, respectively (Bruker Nano GmbH, 2017). Each excitation beam is 10 mm in diameter. The S4 T-STAR was operated with the Mo_K and W_L excitation lines for a measurement time of 500 s each. The software T-ESPRIT was used to process the X-ray spectra, analyse elemental concentrations, and deconvolute spectra peaks for element identification. This spectrometer has a capacity of 90 samples and can theoretically analyse elements from sodium (Na) to uranium (U).

3.5.7 Sample measurement

Each prepared sample was orientated at a particular angle and measured for 500 s. Subsequently, it was rotated by 90° and remeasured. Measuring at different angles ensured that, in situations where the sample diameter extended beyond the recommended 10 mm (X-ray beam diameter), the rotation will allow the sample outside the centre to be measured. As such, the possibility of effectively analysing the whole sample is enhanced. An average of the two measurements was then used in post analysis. Since quartz sample carrier discs and filters were used, silicon was not considered in the data interpretation.

3.6 Ion analysis

Samples were prepared for the analysis of water-soluble ions in PM₁₀ particles, and their ionic constituent concentrations quantified by ion chromatography (IC).

3.6.1 Sample preparation

Sample filters were sub-sampled by punching out three spots of 20 mm diameter using a ceramic puncher. Punched filter spots were transferred into 50 ml sample vials and extracted with 20 ml deionised water (18.2 MΩ cm, Milli-Q system, Merck Millipore) by shaking for 2 hrs. A 0.45 µm one-way disposable syringe filter was then used to filter the extract to remove insoluble particles prior to the IC measurement. Field blanks used for blank correcting the sample concentrations were also prepared in the same way.

3.6.2 Analytical method and sample measurement

Ion chromatography is a method for separating and quantifying different ions from a mixture. The basis for the separation lies in the difference in ionic charge of distinct compounds, which define different travel rates through certain materials (Chagué-Goff & Wong, 2013).

In IC analysis, a sample is loaded into a sample loop via an injector. The sample is then pushed ahead into an analytical column by an eluent (mobile phase) delivered by a pump. The column is packed with a gel-like or solid material such as resin. This packing is referred to as the stationary phase. Before reaching the column, the analyte passes through a guard column where unwanted substances are removed. Inside the column, ionic components are separated depending on their partitioning between the mobile and stationary phases. As the eluent continuously flows through the column, different constituents travel along at varying rates depending on their affinity for a specific phase. Components with high eluent affinity are eluted first as they flow faster while those with low affinity are eluted later. Components are therefore detected as they exit the column at different times, known as their retention times in the column. Afterwards, the separated components move through a membrane device (suppressor) to the detector. The suppressor limits background noise and enhances detection. The detector, typically a conductivity cell, detects ionic components to generate a series of peaks (chromatogram) displayed on a connected computer. A schematic of the basic setup of the chromatography system is shown in Fig. 3.

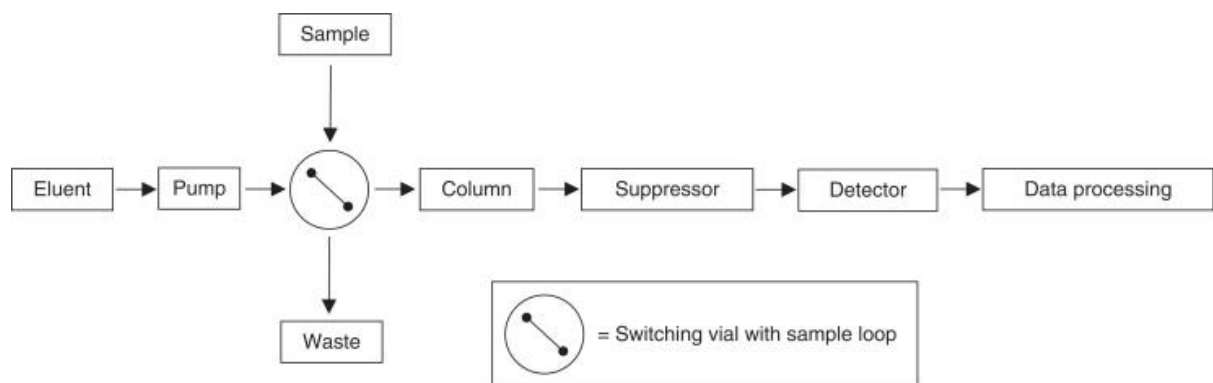


Figure 3. Schematic of the setup of an ion chromatograph (Source: Chagué-Goff & Wong, 2013).

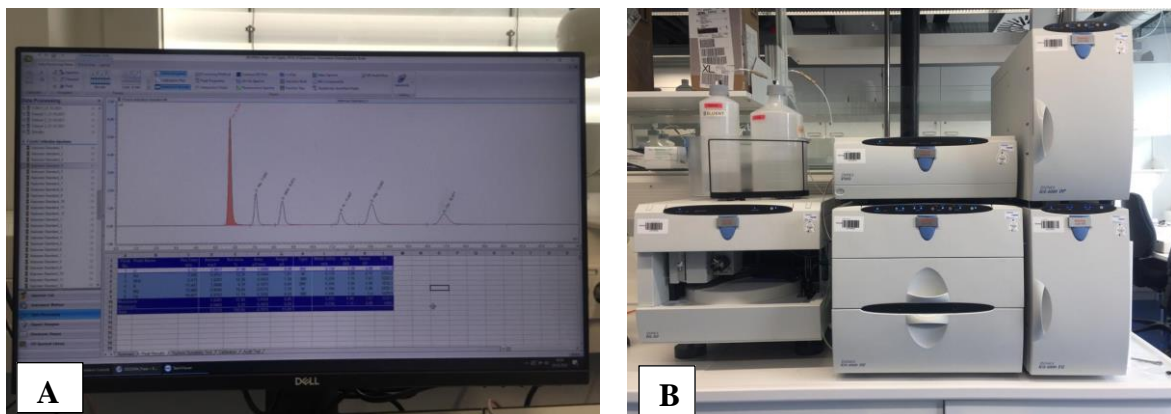


Figure 4. Ion chromatography (IC). An example of a chromatogram displayed on the monitor of a computer during analysis (A). The Dionex IC system used for ion analysis and its accessories (B).

The chromatogram (Fig. 4-A) is displayed on a connected computer. Such computers have software that automatically identifies ionic species by comparing measured travel times with pre-defined species retention time. The concentration of each detected species is quantified using area under the peak or the peak height.

3.6.3 Measurement instrument

A Dionex ICS-6000 dual channel ion chromatograph (Thermo Scientific, USA) was used for simultaneous analysis of cations and anions (Fig. 4-A). This instrument is equipped with dual pumps, a micro membrane suppression device, and it automatically prepares eluent using Reagent-Free Ion Chromatography-Eluent Generation (RFIC-EG). The eluents used for cation and anion exchange were methanesulfonic acid (MSA) and potassium hydroxide (KOH), respectively (Fomba et al., 2014). To separate anions, a combination of AG18 and AS18 (2 mm) analytical columns were used, while cation analysis was carried out with CG16 and CS16 (3 mm) columns (Fomba et al., 2019; Deabji et al., 2021). Additionally, the instrument was coupled with an AS-AP autosampler that held the sample vials. Conductivity measurements by the instrument were then analysed on a connected computer using the software Chromeleon 7.3. The computer also facilitated the viewing of generated chromatograms.

3.7 Elemental carbon analysis

Data on elemental carbon (EC) concentrations determined from the filter samples were obtained from the atmospheric chemistry department (ACD) of the Leibniz Institute for Tropospheric Research (TROPOS). The EC measurement was performed on cut-off filter pieces (1.5 cm²) using a dual carbonaceous analyser (Sunset Laboratory Inc., USA), with a thermo-optical method following the EUSAAR (European Supersites for Atmospheric Aerosol Research) –2 protocol. Further details of the analytical procedure are provided in Deabji et al. (2021).

3.8 Data analysis

For the data analysis carried out during this work, if not indicated otherwise, the freely available software R (version 4.1.0) was utilised.

3.8.1 Calculation of atmospheric concentrations

The atmospheric concentration of the chemical species was computed after obtaining the elemental and ionic mass concentrations from the extract. Corresponding mass concentrations

for each species obtained from the field blanks were subtracted from the extract mass concentration of the samples to derive their blank corrected mass concentration.

- **Trace metals**

The blank corrected extract concentrations of the trace metals were converted to atmospheric concentrations by applying eqn. (2).

$$C_E = \frac{M_C * D_F * F_R}{V_A} \quad (2)$$

Where C_E is the atmospheric concentration of the element; M_C is the element mass concentration in the PM_{10} extract; D_F is the dilution factor (ratio of the digesting solution volume to the sample volume); V_A is the volume of air sampled (computed as product of sample duration time and air-flow rate); F_R is the ratio of the total filter area to the total sub-sampled filter area.

- **Ions**

The blank corrected extract concentrations of the ions were converted into atmospheric concentrations by applying eqn. (3).

$$C_I = \frac{M_C \times V_E}{V_A} \times F_R \quad (3)$$

Where C_I is the atmospheric concentration of the ion; M_C is the ion mass concentration in the PM_{10} extract; V_E is the volume of the extract, V_A is the volume of air sampled and F_R is the filter ratio. The parameters V_A and F_R are computed in the same way as in eqn. (2).

3.8.2 Determination of PM_{10} source regions

The source regions of air masses arriving at the CVAO were investigated by performing back trajectory analysis to help interpret data on PM_{10} samples. Back trajectories provide information not only about the travel direction of an air parcel at a certain point but also about where the air has been (Stein et al., 2015). Trajectories were computed using the TrajCalc software (van Pinxteren et al., 2010) used internally at the atmospheric chemistry department of TROPOS. TrajCalc is a PC version of the Hybrid Single-Particle Lagrangian Integrated Trajectory (HYSPLIT) model (version 4.9) developed by the National Oceanic and Atmospheric Administration's (NOAA) Air Resource Laboratory (ARL).

Meteorological data used for the model run was output from the Global Data Assimilation System (GDAS). The dataset has a spatial and temporal resolution of 1° and 3 hr, respectively. It was obtained from the GDAS archive on the ARL server (<ftp://ftp.arl.noaa.gov/archives/gdas1>, last access: 25th July, 2022) using a file transfer protocol (FTP). The model was used to compute 96 hr backward trajectories with 6 hr intervals at a starting altitude of 500 m above ground level. It automatically calculated vertical velocity using the vertical velocity fields that came along with the input data (default option).

The trajectories were then clustered to identify distinct transport categories. The ideal cluster number was selected after an iterative testing of three to seven clusters. Each output was evaluated based on the distinct geographical origin of each air mass cluster. In clustering, the difference between constituent trajectories of a cluster is reduced while the difference among clusters is maximised.

3.8.3 Estimation of dust

The mass concentration of the mineral dust component of PM was estimated by applying the following formula (Deabji et al., 2021):

$$[MD] = 1.16 * (1.9 * [Al] + 23.3 * [Ca] + 2.09 * [Fe] + 1.67 * [Ti]) \quad (4)$$

Where [MD] is the estimated concentration of mineral dust, while [Al], [Ca], [Fe] and [Ti] are the measured mass concentrations Al, Ca, Fe, and Ti, respectively.

3.8.4 Estimation of non-sea salt potassium

The mass concentration of the non-sea salt potassium (nss-K⁺) component of PM was estimated by applying the following formula (Song et al., 2018):

$$[nss - K^+] = [K^+] - 0.037 * [Na^+] \quad (5)$$

Where [nss-K⁺] is the estimated concentration of nss-K⁺, while [K⁺] and [Na⁺] are the measured mass concentrations of K⁺ and Na⁺, respectively.

3.8.5 Calculation of nutrient deposition fluxes

The atmospheric deposition fluxes of PM nutrients to the ETNA ocean surrounding the Cape Verde Islands were estimated by applying eqn. (6). Only dry deposition was estimated as Fomba et al. (2014) has expressed that wet deposition fluxes in this region are low.

$$F_D = V_D \times C_S \quad (6)$$

Where F_D is the estimate of the dry deposition flux of a specie; C_S is the calculated atmospheric concentration of the specie and V_D is the deposition velocity of the specie. The depositional velocities were estimated for PM_{10} samples based on eqn. (7); W_S is the average wind speed over each sample's sampling time frame. The equation was established by Niedermeier et al. (2014), who investigated different methods for estimating depositional fluxes of mineral dust to the ETNA using data from the CVAO

$$V_D = 0.5214 \times e^{0.0541 \times W_S} \quad (7)$$

4. Results and Discussion

4.1 Chemical composition of PM₁₀

Over the study period, 420 filters were collected and analysed to determine the chemical composition of the PM₁₀ samples. Water-soluble ions were analysed from all filters, but only samples from 2017 and 2018 were used for trace metal analysis. Table 2 presents a statistical summary of the mass concentration of PM₁₀ and some of its measured chemical components. The results showed high variation in species concentration. A complete summary of all chemical species analysed is found in Appendix A. From here on, the primary focus of the results will be on the major nutrients (NO₃⁻, NH₄⁺, and PO₄³⁻) and bioactive trace elements (Al, Fe, Mn, V, Zn, Ni, Cu).

Table 2. Statistical summary of the mass concentration of particulate matter (PM₁₀), select water-soluble ions and trace metals from the list of chemical components analysed in aerosol samples collected over the study period (2017 - 2019). Aerosols sampled in 2019 were not considered in obtaining trace metal values.

	Unit	Minimum	Maximum	Mean	SD
PM ₁₀ mass	µg/m ³	8.57	547.94	51.87	57.56
NO ₃ ⁻	µg/m ³	0.00	2.41	1.11	0.47
SO ₄ ²⁻	µg/m ³	0.00	7.68	2.36	1.10
NO ₂ ⁻	ng/m ³	0.00	10.23	0.16	0.71
PO ₄ ³⁻	ng/m ³	0.00	61.31	3.09	5.85
Na ⁺	µg/m ³	0.32	8.73	3.71	1.36
NH ₄ ⁺	µg/m ³	0.00	0.18	0.03	0.03
K ⁺	µg/m ³	0.00	0.53	0.17	0.08
Al	µg/m ³	0.00	29.08	1.38	2.54
P	µg/m ³	0.00	2.37	0.04	1.16
V	ng/m ³	0.11	44.79	4.03	5.60
Mn	µg/m ³	0.00	0.41	0.03	0.05
Fe	µg/m ³	0.00	23.18	1.58	2.81
Ni	ng/m ³	0.00	62.83	2.65	7.52
Cu	ng/m ³	0.00	8.88	0.61	1.14
Zn	ng/m ³	0.00	104.45	6.47	10.67

The concentrations of the aerosol nutrients followed a descending order of: Fe > Al > NO₃⁻ > Mn > NH₄⁺ > Zn > V > PO₄³⁻ > Ni > Cu (Table 2). On average, NO₃⁻ and NH₄⁺ accounted for 91.9 % and 8.0 % of the total inorganic N, respectively. In addition, their concentrations were at least two orders of magnitude greater than that of PO₄³⁻. The concentrations of Fe, Mn and Al were considerably higher than those of the other trace elements, indicative of a high emission source. In general, the mean elemental concentrations were comparable to those reported in previous studies conducted in the tropical North Atlantic (Gelado-Caballero et al., 2012; Johansen et al., 2000; Patey et al., 2015). The concentrations of NH₄⁺ and NO₃⁻ were similar to those reported by Fomba et al. (2014) at the CVAO. However, the mean NH₄⁺ concentration (0.18 µg m⁻³) from Johansen et al., (2000) was six times higher than that in this work, whereas their NO₃⁻ concentration (0.67 µg m⁻³) was not that different. Assessing the chemical composition of aerosols is important for identifying sources and processes that influence the concentration of component species (Priyadarshini et al., 2019)

4.2 Mass concentration of PM₁₀

4.2.1 Temporal variation

Figure 5 displays the interannual trends of PM₁₀ mass concentrations at the CVAO. Each year, the temporal variation of the PM₁₀ load was different. In 2017, consistently higher mass concentrations were noted in the latter parts of the year. This trend was reversed in 2019, with higher concentrations observed in the early part of the year. Across all years, relatively lower concentrations were observed in the mid-year, although sporadic peaks were seen in 2018. The annual average mass concentrations for 2017, 2018 and 2019 were 55.8 ± 52.3 µg m⁻³ (ranging from 9.1 to 330.7 µg m⁻³), 41.9 ± 38.1 µg m⁻³ (ranging from 9.8 to 286.1 µg m⁻³) and 56.5 ± 72.4 µg m⁻³ (ranging from 8.6 to 547.9 µg m⁻³), respectively. During the study period, 14.1 µg m⁻³ was found to be representative of the baseline conditions, which is the lower 5th percentile of PM₁₀ concentrations (Deabji et al., 2021).

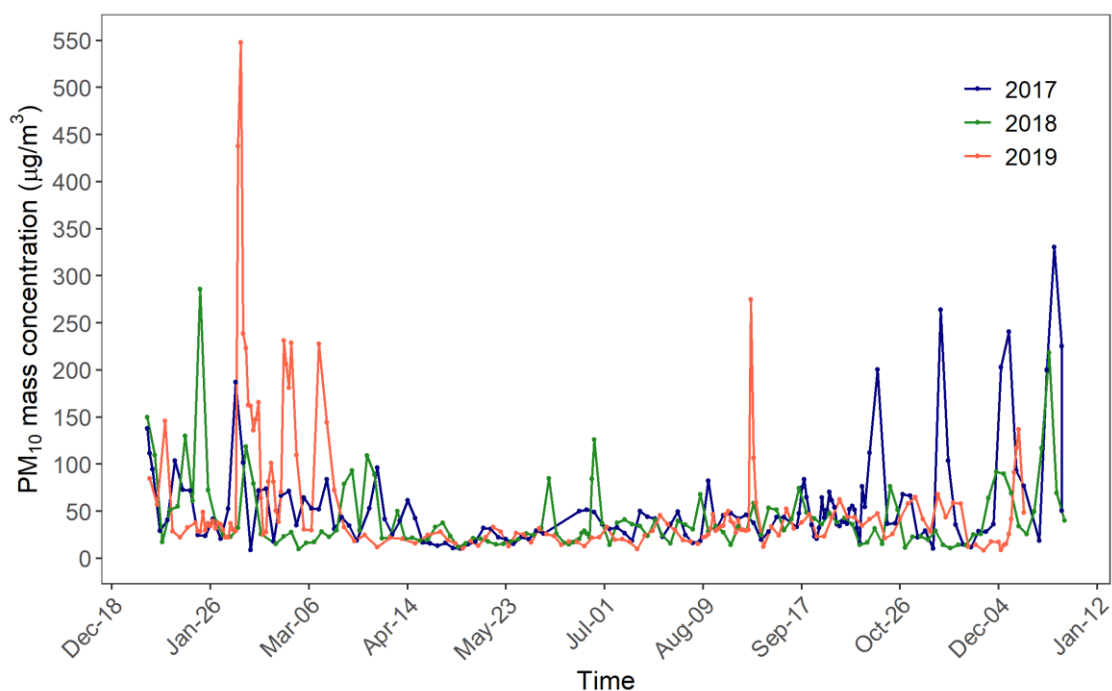


Figure 5. Annual variability of PM₁₀ mass concentration during the study period.

The strong temporal variability observed aligns with findings from other studies that have characterised the variations in aerosol particle loading over the region (Fomba et al., 2014; Gama et al., 2015). Additionally, the average yearly PM concentrations reported here and in the referenced studies are similar and range between $42 \mu\text{g m}^{-3}$ and $57 \mu\text{g m}^{-3}$.

4.2.2 Seasonal variation

The seasonal variability of PM₁₀ mass loading at the CVAO during the study period was investigated and is presented in Fig. 6. The PM₁₀ mass concentrations show clear seasonal variations, with the lowest monthly mean concentrations recorded during late spring to summer (April to August) and in November. Winter was identified as the period with the highest PM₁₀ concentrations, with the predominant month varying between December (2017), January (2018), and February (2019) depending on the reference year. The mean PM₁₀ mass loading for winter, spring, summer, and autumn were found to be 88.1 ± 87.1 , 34.2 ± 32.3 , 35.6 ± 29.3 and $43.6 \pm 33.3 \mu\text{g m}^{-3}$, respectively, resulting in a 60% decrease in PM₁₀ concentration from winter to summer.

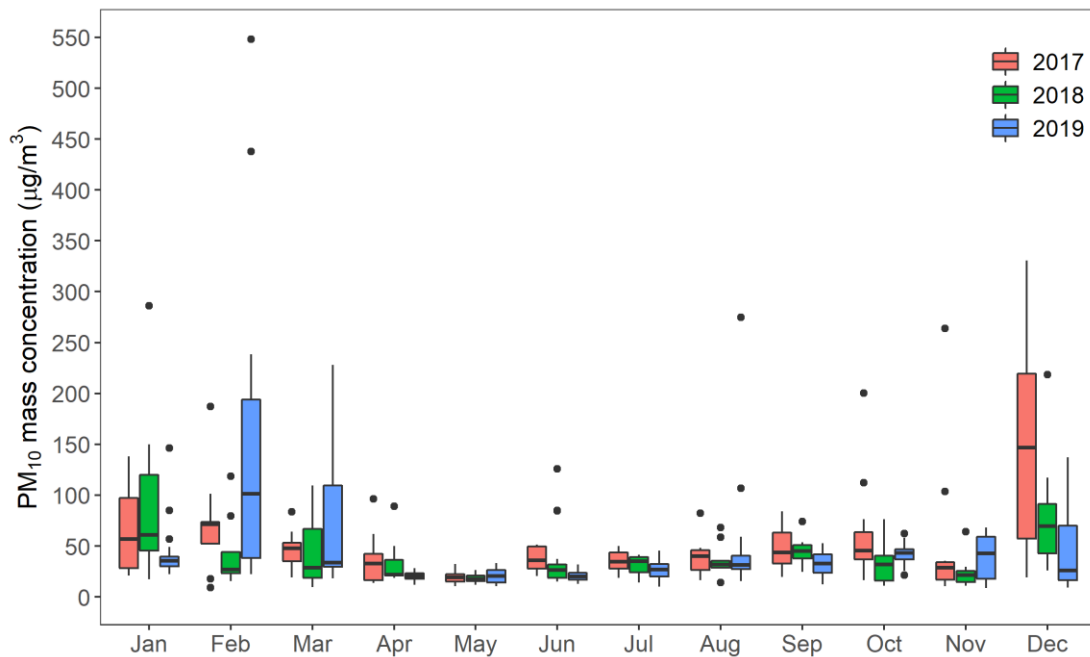


Figure 6. Boxplots of the monthly particulate matter (PM₁₀) mass concentration for the three years (2017, 2018, and 2019). Boxes show interquartile range and the horizontal bar in each box shows the median. Upper and lower limits of the whiskers represent the 90th and 10th percentiles of the data. Black dots are the extremes (values greater or less than 1.5 times the interquartile range above or below the upper and lower quartiles, respectively).

This seasonal pattern was in line with previous studies in the Cape Verde region, which reported highest concentrations in winter and lowest in spring and summer (Fomba et al., 2014; Gama et al., 2015; Patey et al., 2015). The average seasonal mass concentrations in this study were also similar to those reported by (Fomba et al., 2014).

Shifts in the northeast trade winds and the Saharan Air Layer (SAL) — factors which play a role in regulating northwest Africa's atmospheric circulation (Castillo et al., 2017) — have been noted to drive the seasonal changes in PM concentrations over Cape Verde. The Cape Verde Islands are situated on the path of Saharan dust export to the North Atlantic. Thus, aerosol particle loading over the area is influenced by the seasonal fluctuations in dust transport. In winter, the trade winds transport Saharan dust close to surface levels, leading to increased PM concentrations over Cape Verde (Schepanski et al., 2009). The Bodélé Depression, the world's dominant dust source, also contributes to the transported dust during this season (Carpenter et al., 2010). In contrast, summer dust transport occurs within the elevated SAL above the trade winds inversion, resulting in low PM concentrations over the islands. In fall, sporadic turbulence in the SAL can cause episodic dust events at near-surface levels (van Pinxteren et al., 2020). Finally, spring is characterised by a transition from lower transport layers in winter to higher layers in summer (Schepanski et al., 2009).

4.3 Air masses

4.3.1 Cluster analysis

A total of 4548 96-hr back trajectories were generated for the 420 samples collected at the CVAO over the 3-yr sampling period. Some of these trajectories (684) had highly mixed origins and were therefore excluded from the cluster analysis. From the remaining trajectories, a four-cluster solution was determined as the ideal outcome of the cluster analysis. Each cluster was depicted by a unique profile and geographical origin (Fig. 7).

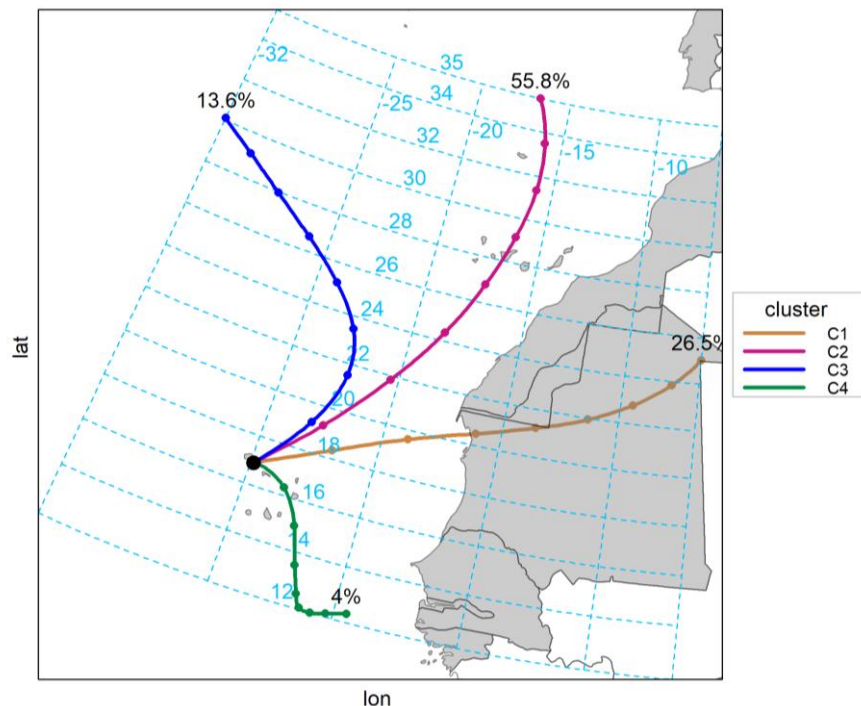


Figure 7. Distinct air mass clusters (4) obtained from the clustering of all 96-hr backward trajectories ending at the Cape Verde Atmospheric Observatory (CVAO) during the study period. The percentages shown represent the proportion of total trajectories in each cluster.

Therefore, based on the profiles and origins, the source regions, represented by the clusters were described as: i) Sahel-Sahara Africa (SSA): air masses from the Sahel-Sahara Desert region, crossing coastal areas in northwest West Africa, the Mauritanian upwelling region, and the ocean to CVAO; ii) Atlantic Coastal Europe (ACE): air masses from off the coast of southwest Europe, passing over the Canary Islands and the ocean to CVAO; ii) Atlantic Marine (ATM): air masses from the northwestern North Atlantic exclusively spending the 96-hr before arriving at the CVAO over the ocean; and iv) Coastal Africa and Atlantic (CAA): air masses from coastal areas of West Africa (Senegal, Gambia, Guinea Bissau) and spending a relatively considerable time over the North Atlantic.

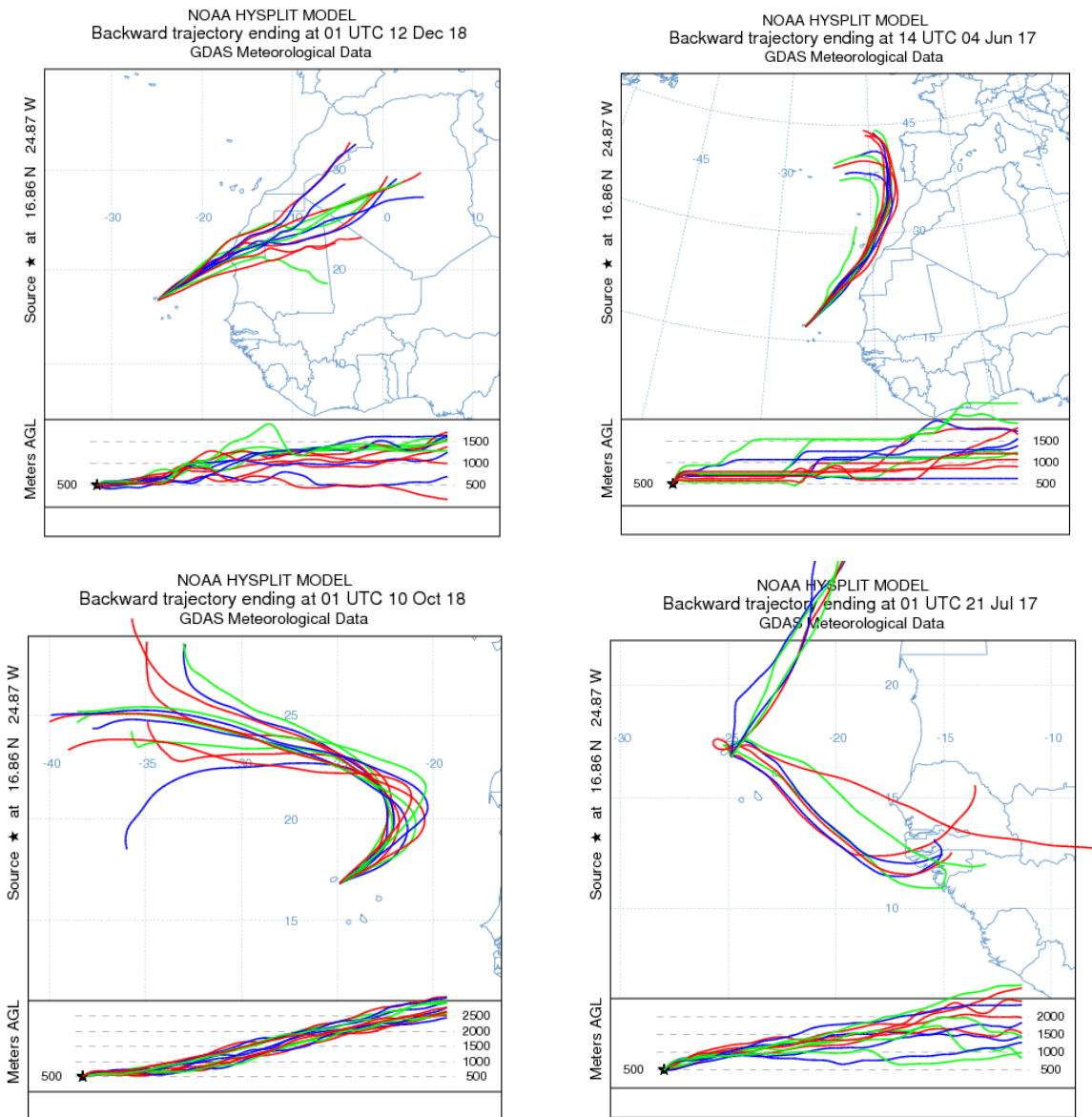


Figure 8. Typical 96-hr back trajectories at 6-hr intervals representative of the identified air mass categories Sahel-Sahara Africa — SSA (top-left), Atlantic Coastal Europe — ACE (top-right), Atlantic Marine — ATM (bottom-left) and Coastal Africa and Atlantic — CAA (bottom-right).

Examples of 96-hr back trajectories typical of each air mass category are shown in Fig. 8. Furthermore, Fig. 8 shows that the air masses travelled over 500 km before reaching the CVAO. Overall, over half of all air masses came from the ACE region, followed by those from the SSA area, then the ATM region and lastly, the CAA area.

4.3.2 Seasonal changes in air mass origin

Additionally, the trajectories were clustered per season to explore seasonal changes in the origin of the air masses arriving at the CVAO. Figure 9 shows the air masses and how their mean trajectories originating from different regions vary over the seasons. Within each season, the

mean trajectories describe a distinct path. In winter, a high percentage (50.2 %) of air masses were derived from the Sahel-Sahara region of Africa. In spring and summer, air masses mostly arrive from off of southwest Europe. Furthermore, spring reveals a minor contribution from northwest Sahara (9.6 %), while the summer contribution from Africa is restricted to coastal areas. Across all seasons, only autumn showed a contribution (3 %) of air masses from the southern tropical North Atlantic region.

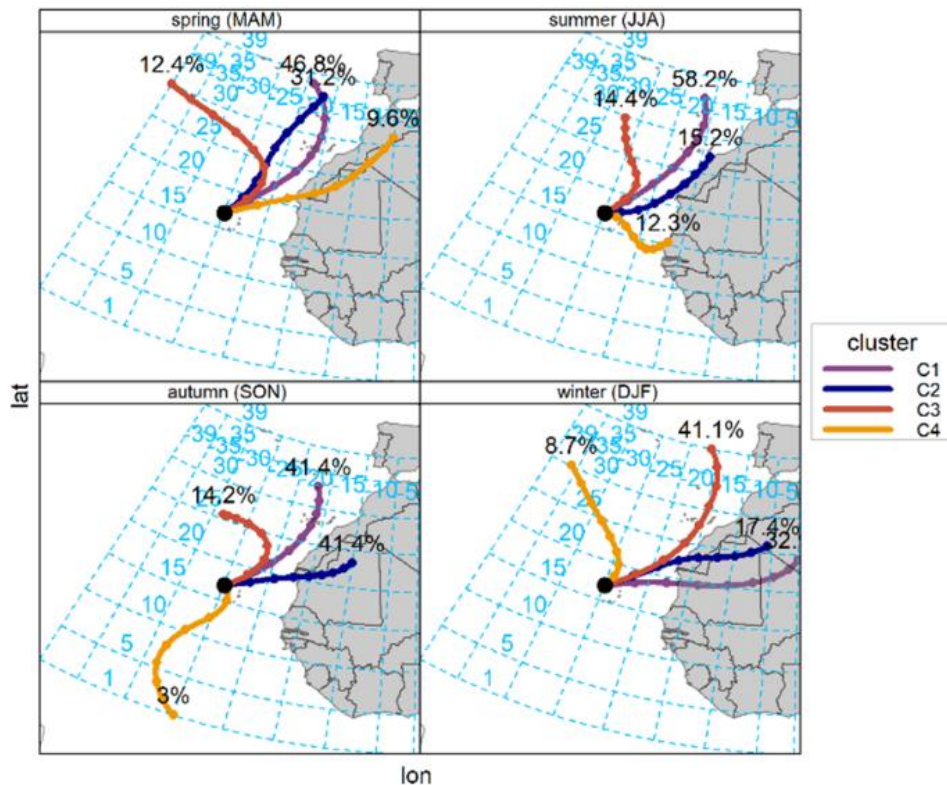


Figure 9. Seasonal changes in the air mass clusters (Cluster 1 — C1, Cluster 2 — C2, Cluster 3 — C3 and Cluster 4 — C4) influencing the Cape Verde Atmospheric Observatory over the sampling period.

The seasonal variation in the origin of air masses affecting the Cape Verde region has been linked to the anticyclonic flow of the Azores high-pressure system (Carpenter et al., 2010). The Azores high occurs north of the Cape Verde Islands. As the structure and position change with the seasons, its associated northeast airflow passes over different regions. During winter, the Azores high is wider, extending from the Caribbean to the Middle East. In this scenario, air masses flowing to Cape Verde have a substantial contribution from the African continent. In summer, the situation created by the shrinking and limitation of the pressure system to the central Atlantic results in air masses flowing from coastal Africa and Europe.

4.4 Nutrient sources

4.4.1 Contribution of source regions

The nutrient species were classified according to the relative contribution of each defined source region to the observed concentration. This is shown in Fig. 10. The SSA region was the main contributor to the concentrations of NO_3^- , soluble (PO_4^{3-}) and total P, as well as all micronutrients (Al, Fe, Mn, V, Ni, Cu, and Zn). The contributions ranged from 38.8 % to 59.8 %. Contribution to NH_4^+ levels was highest for CAA (36.1 %). In the case of Al, Fe, Mn, and V, SSA's contribution was more than twice that of the next contributor (CAA). For the nutrients Ni, Cu, Zn, NO_3^- , and PO_4^{3-} , although the percentage contributions from the SSA region were higher, they were relatively similar to those of the CAA region. Furthermore, apart from NH_4^+ and total P, the CAA region was the second most important contributor to the concentrations of all other species. Surprisingly, although ACE (29.4 %) contributed more to total P than CAA (14.2 %), this did not translate into a higher contribution to PO_4^{3-} . Instead, the contribution from the CAA region (33.4 %) was higher. Also, despite CAA air masses contributing the least to total P, their contribution to PO_4^{3-} was comparable to SSA air masses (36.4 %), highlighting the importance of the source that enriched CAA air masses with PO_4^{3-} . Overall, the nutrient contribution was dominated by long range transport from the African continent.

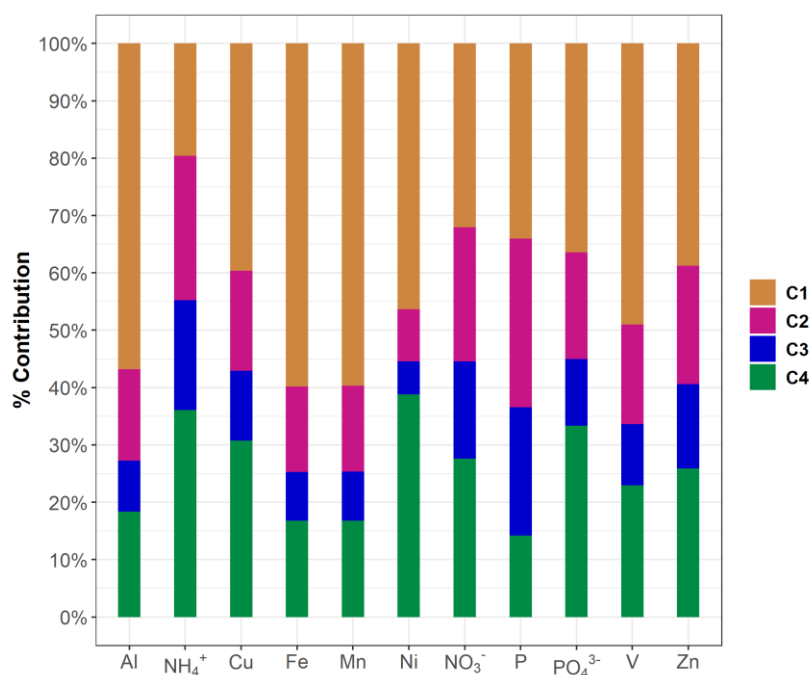


Figure 10. Relative contribution of the four identified source regions (Sahel-Sahara Africa (C1), Atlantic Coastal Europe (C2), Atlantic Marine (C3) and Coastal Africa and Atlantic (C4)) to concentrations of nutrient species observed at the Cape Verde Atmospheric Observatory over the study period.

4.4.2 Species interrelationship

Correlation analysis was performed to investigate the interrelationship between nutrients, nss-K⁺ and the dust component of PM. The result is shown in Fig. 11. Generally, significantly good correlations were observed between most of the PM components. The results revealed that mineral dust, Al, V, Mn and Fe exhibited very strong correlations with each other, with coefficients above 0.9. This suggested that dust was the source of Al, Mn and Fe, and also contributed to the budget of elements such as V. The PO₄³⁻ and nss-K⁺ components presented their lowest coefficients with Cu, Zn and Ni, signalling that the pair of PO₄³⁻ and nss-K⁺ and the species Cu, Zn and Ni, were not of a common origin. Notably, NH₄⁺ showed very weak correlations with all other components (coefficients < 0.2). This suggested that the main source or reaction process producing NH₄⁺ did not contribute to the other species. Accordingly, for NH₄⁺ and NO₃⁻, the correlation observed could be a reflection of the instability of ammonium nitrate at relatively high temperatures. In literature, correlation coefficients have often been used to gain information on potential common aerosol component sources. However, for long-range transported species, these coefficients may not provide robust information due to the influence of meteorological conditions and mixing during transport on the interrelationships between species, which may outweigh the effects of source similarity.

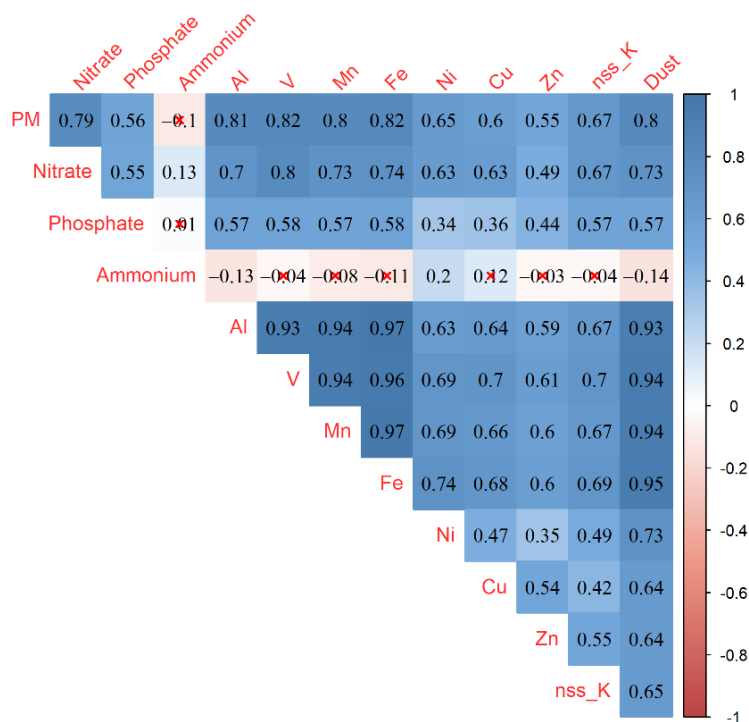


Figure 11. Correlation coefficients of nutrient species, non-sea salt potassium (nss_K), and dust component of aerosol particles collected at the Cape Verde Atmospheric Observatory. Correlations are significant at the 0.05 level (pairwise) in all boxes except those marked with a red cross.

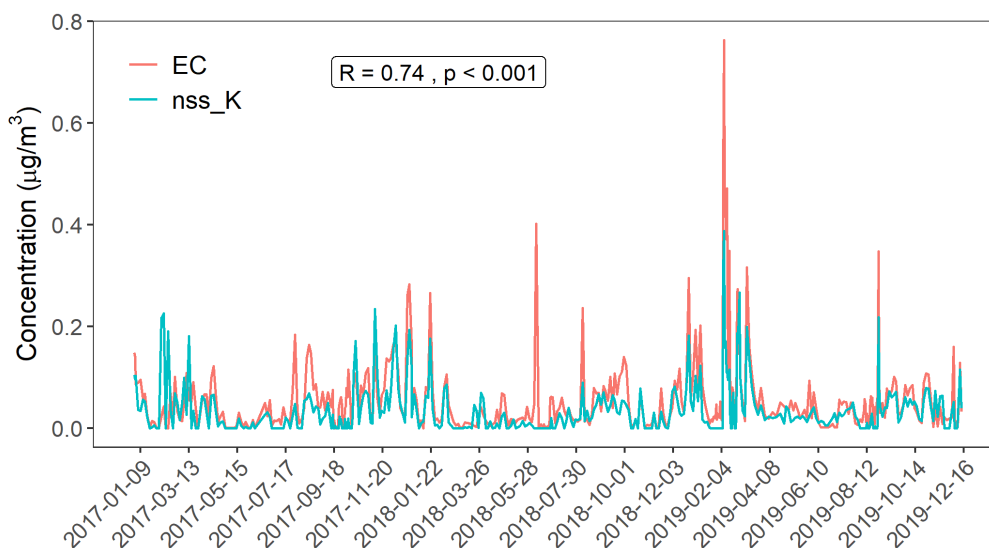


Figure 12. Time series of elemental carbon (EC) and non-sea salt potassium (nss_K) measured during the study period.

4.4.3 Source markers

- ***Biomass burning***

The effect of biomass burning on the collected aerosol particles was assessed using the biomass burning tracer nss-K⁺ (Song et al., 2018; Zong et al., 2016). The temporal variation of nss-K⁺ was coupled with that of EC, a common biomass burning aerosol, as presented in Fig. 12. Their similar variability and significantly good correlation ($r = 0.74$, $p < 0.001$) was a strong indication of the influence of biomass burning on sampled aerosol particles.

Furthermore, seasonality in the relative influence of biomass burning emission was investigated by employing the nss-K⁺ to K⁺ ratio in the aerosols as a proxy (Song et al., 2018). The result is presented in Fig. 13. The concentration of nss-K⁺ ranged from 0 – 0.39 $\mu\text{g}/\text{m}^3$ (mean: $0.03 \pm 0.05 \mu\text{g}/\text{m}^3$) and described 0 – 73 % of the total K⁺. Strong biomass burning emissions (relatively high ratios) were evident in winter — the West African dry season — while reduced emissions (low ratios) were observed in summer — the West African wet season. Also, in terms of source regions, the mean nss-K⁺ to K⁺ ratio for air masses arriving from SSA, CAA, ACE and ATM were 0.28, 0.18, 0.13 and 0.12, respectively. It is noted that in addition to biomass burning, nss-K⁺ also has crustal sources. But, in this study, it was assumed that the nss-K⁺ concentration was primarily from biomass burning.

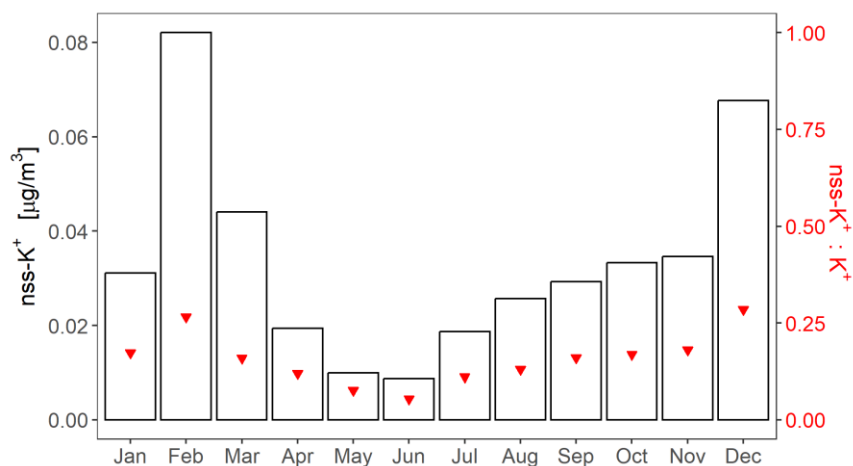


Figure 13. Monthly mean non-sea salt potassium (nss-K⁺) to potassium (K⁺) ratio (denoted as inverted triangles) and nss-K⁺ concentration (denoted as bars).

- *Ship emissions*

The influence of ship emissions was observed using the V to Ni ratio. Zong et al. (2016), reported that ship emissions are characterised by a V / Ni ratio above 0.7. Figure 14 depicts the monthly variation of the calculated V / Ni ratio in sampled aerosols. It was evident that emissions from ships affected collected aerosols throughout the year. Many coastal routes exist along the coast of North and West Africa, while there are major sea lanes passing through the Cape Verde region. Emissions along these routes can thus enrich transported aerosol particles. These metals may also have been derived from oil combustion emissions in urban cities in West Africa. Seasonally, the emissions were pronounced in summer and reduced from December – April. This may possibly be linked to seasonal changes in maritime trade or cruise tourism in Europe.

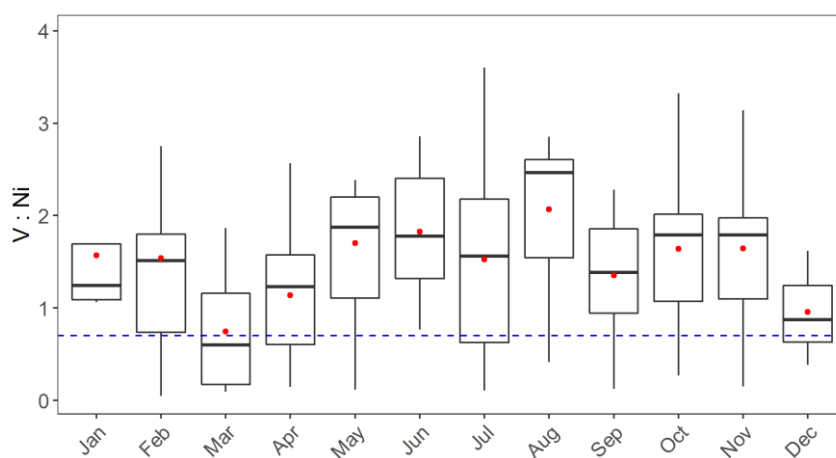


Figure 14. Boxplots of monthly V to Ni ratio. Red dots represent the mean, and the dashed blue line is the minimum threshold ratio (0.7) that signals the influence of ship emission.

The sources of deposited nutrients were identified based on the following: clustering back trajectories to identify source regions, assessing the relative contribution of the source regions to measured concentrations, as well as analysing specific source markers and the interrelationship between species. The results revealed a mixed pattern of influence from natural and anthropogenic emissions on the budget of atmospheric nutrient input to the ETNA. Additionally, the long distance (> 500 km) travelled by the air masses meant that the species they carried were well mixed during transport, and this may dampen unique source signals.

With the exception of NH_4^+ , all investigated species had a significant association with mineral dust from the Sahel-Sahara region. Mineral dust was also co-transported with anthropogenic aerosols. The bioactive elements Al, Fe, and Mn are major components of Saharan dust (Fomba et al., 2013). Their strong relationship with each other and mineral dust demonstrated their utility as dust tracers. For dust derived nutrients, their fractional solubility is low (Mahowald et al., 2018). Guo et al. (2022) reported an inverse relationship between dust and soluble concentrations of Al and Fe. Therefore, during the dust season in winter, fluxes of dust derived elements will likely have lower solubility. It is recognized that Al, Fe and Mn can also have non-crustal sources (Deabji et al., 2021) such as mining and metallurgical activities.

The elements Ni, V, Cu, and Zn, are qualified as proxies for anthropogenic emissions (Deabji et al., 2021; Gelado-Caballero et al., 2012). Hence, their loading in transported particles was probably more controlled by anthropogenic emissions. But, especially for V, whether anthropogenic sources dominated its contribution was unclear as it showed a significantly strong correlation with dust. In this study, anthropogenic emissions were derived from sources in Europe, North America and coastal West Africa. In terms of specific sources, oil combustion from ships ($\text{V} / \text{Ni} > 0.7$; Zong et al., 2016) affected all air masses over the Cape Verde region. For Cu and Zn, they are mainly released from industrial activities (Zong et al., 2018). Therefore, steel and iron producing industries situated in urban cities, including Nouakchott (Mauritania), Banjul (Gambia), and Dakar (Senegal) were key sources. Vehicle emissions are also a source of Zn.

The inorganic nutrients NO_3^- , NH_4^+ , and PO_4^{3-} were mostly emitted from anthropogenic activities, although they also have natural sources. Ocean emissions have been indicated as a source of NO_3^- (Desboeufs et al., 2018, Fomba et al., 2014) and NH_4^+ (Paulot et al., 2015). Deabji et al. (2021) attributed elevated concentrations of NO_3^- at a high-altitude site in Morocco to long-range transport of Saharan dust. Natural soils are also sources of NH_3 (Hickman et al., 2021) and P (Berthold et al., 2019; Tipping et al., 2014). From an anthropogenic perspective,

vehicles emit NO_x (NO and NO_2^- ; Giechaskiel et al., 2019) and NH_3 (Zong et al., 2018), species that serve as the precursors for atmospheric formation of NO_3^- and NH_4^+ , respectively. Biomass burning is also a source of NO_x (Jin et al., 2021) and NH_3 (Zong et al., 2016). In West Africa, agriculture has become an ever-growing source of NH_3 (Hickman et al., 2021). Moreover, atmospheric P can be derived from phosphate manufacturing and coal combustion (Berthold et al., 2019) — activities important in Senegal and Morocco — as well as from biogenic particles and biomass burning (Tipping et al., 2014). This study found that P derived from biomass burning in West Africa had a higher soluble fraction compared to P from mineral dust. Barkley et al. (2019) also reported a similar relationship between the solubility of P from biomass burning and natural sources. Overall, these results suggest that biomass burning aerosols may have played a major role in enriching the PO_4^{3-} content of transported particles.

4.5 Nutrient deposition

The following plots for nutrient fluxes were produced by grouping the major nutrients together and organising the trace elements based on similar potential sources and the magnitude of their flux.

4.5.1 Temporal variation

The time series of the estimated deposition fluxes for the bioactive elements (Al, Fe, Mn, Zn, V, and Cu) and major nutrients (NO_3^- , NH_4^+ , and PO_4^{3-}) are presented in Figs. 15, 16, 17, and 18. Among the trace elements, higher fluxes were observed for Al, Mn, and Fe. Trends in the strong temporal variation of Al, Mn, Fe, V, and Zn fluxes were mostly consistent with each other (Figs. 15, 16, and 17). The overall average deposition flux estimated for the displayed period was $3.39 \pm 5.87 \mu\text{mol}/\text{m}^2/\text{d}$, $1.87 \pm 3.20 \mu\text{mol}/\text{m}^2/\text{d}$, $0.03 \pm 0.06 \mu\text{mol}/\text{m}^2/\text{d}$, $6.66 \pm 10.65 \text{ nmol}/\text{m}^2/\text{d}$, $5.25 \pm 6.86 \text{ nmol}/\text{m}^2/\text{d}$ and $0.65 \pm 1.24 \text{ nmol}/\text{m}^2/\text{d}$ for total Al, Fe, Mn, Zn, V and Cu, respectively. These high standard deviations on the average fluxes ($> 150\%$) already point to the impact of intermittent high deposition events. In the case of major nutrients, the highest fluxes were recorded for NO_3^- and NH_4^+ compared to PO_4^{3-} . The time series of fluxes were highly variable (Fig. 18). Over the displayed period, mean deposition flux estimated was $1.21 \pm 0.51 \mu\text{mol}/\text{m}^2/\text{d}$, $0.11 \pm 0.11 \mu\text{mol}/\text{m}^2/\text{d}$, $0.002 \pm 0.004 \mu\text{mol}/\text{m}^2/\text{d}$ for NO_3^- , NH_4^+ and PO_4^{3-} , respectively.

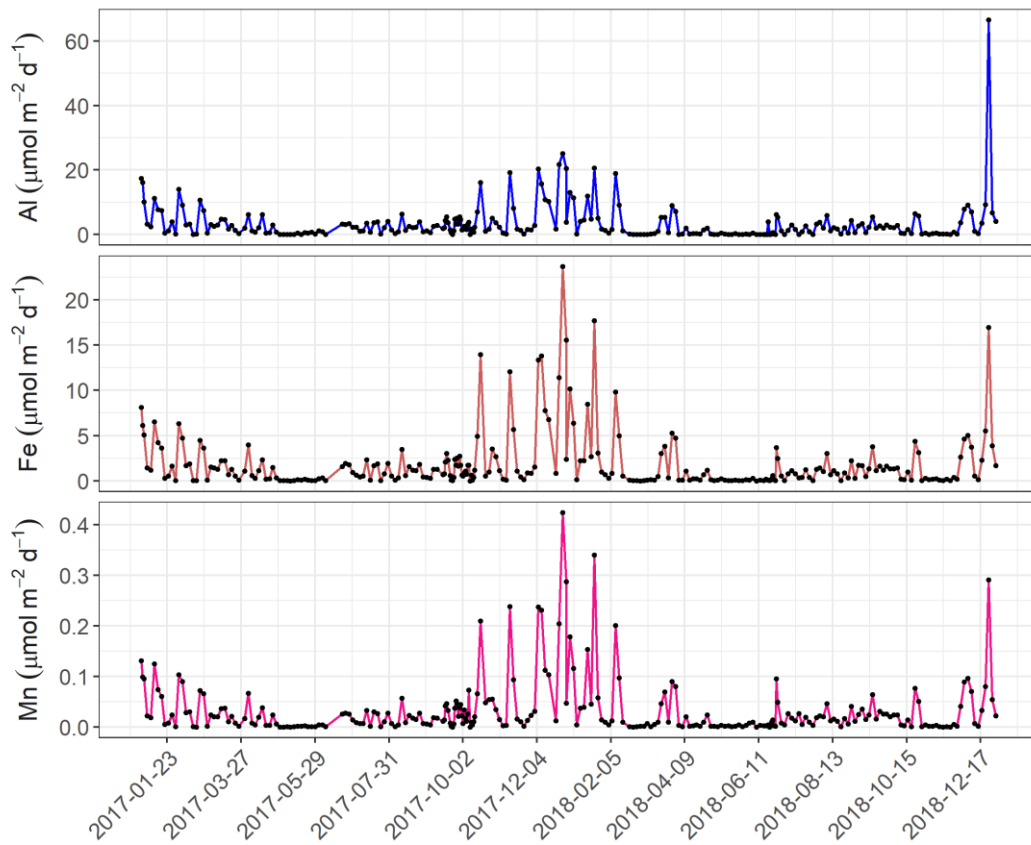


Figure 15. Temporal variation of the nutrient deposition flux of total Al, Fe and Mn.

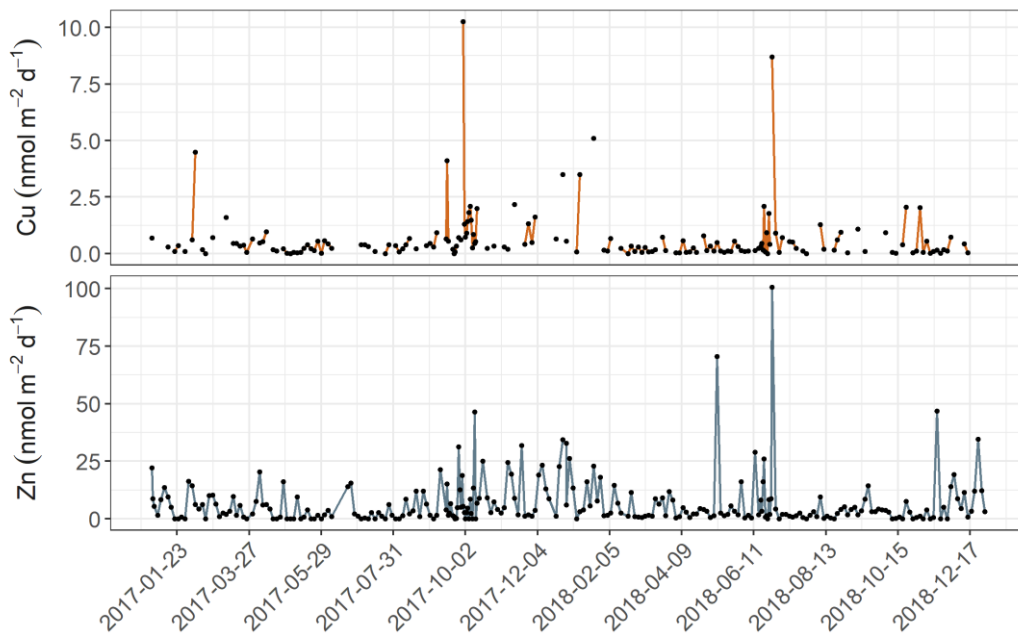


Figure 16. Temporal variation of the nutrient deposition flux of total Cu and Zn.

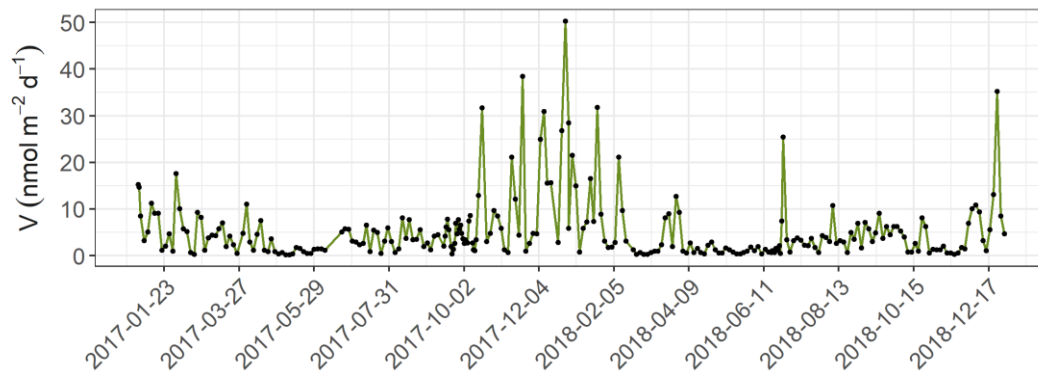


Figure 17. Temporal variation of the nutrient deposition flux of total V.



Figure 18. Temporal variation of the nutrient deposition flux of soluble NO_3^- , NH_4^+ and PO_4^{3-} .

The temporal variation of atmospheric nutrient deposition revealed large differences in the timing of fluxes. Regular instances of relatively high fluxes were observed for all bioactive elements. This can be linked to extreme events, such as dust outbreaks or wildfires — events that are sporadic and induce increased deposition fluxes. Particularly, in the time series of Al, Mn, Fe, Zn and V, the sustained period of elevated fluxes stretching from September 2017 to February 2018 was indicative of major dust storms, consistent with their period of frequent occurrence over Cape Verde. Desboeufs et al. (2018) posited that the effects of nutrient fluxes

derived from episodic events are often short lived. Moreover, since sporadic events cause anomalously high fluxes, continuously emitting sources may be masked.

4.5.2 Seasonal variation

The monthly fluxes of V, Ni, Al, Fe, Mn, Cu, Zn, NO_3^- , NH_4^+ , and PO_4^{3-} , as shown in Figs. 19, 20, 21, and 22, were used to investigate the seasonal variability of nutrient deposition. The monthly fluxes of the nutrient species displayed a marked seasonal pattern. The major deposition fluxes of Al, Fe, Mn, V, and Zn occurred in the winter. For Cu, although higher mean fluxes were usually observed in winter, the maximum monthly mean flux occurred at the beginning of the fall (September; Fig. 21). For Ni, the highest monthly mean fluxes were estimated for July and October (Fig. 19). Additionally, in contrast to the other elements, autumn had the highest average deposition flux (Table 3). For all the investigated micronutrients, the lowest fluxes were observed in May. These seasonal changes in the trace metal fluxes are explained by seasonality in dust outbreaks, which largely control the abundance of aerosol particles over the CVAO.

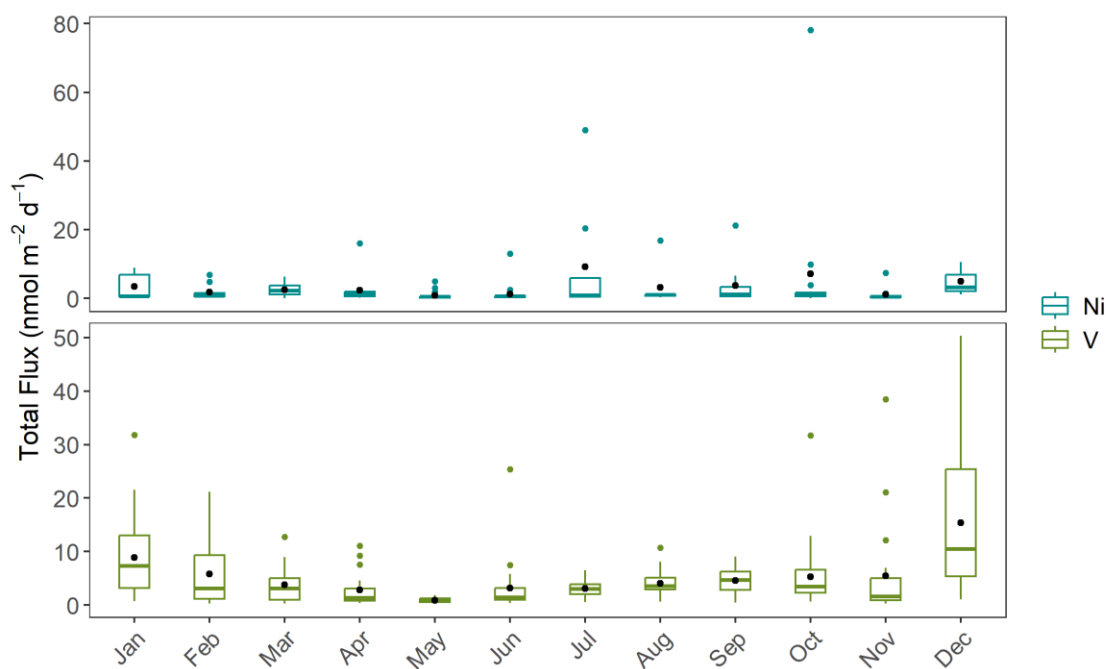


Figure 19. Boxplots of monthly deposition fluxes of total Ni and V. Black and non-black dots represent the mean and extreme values, respectively.

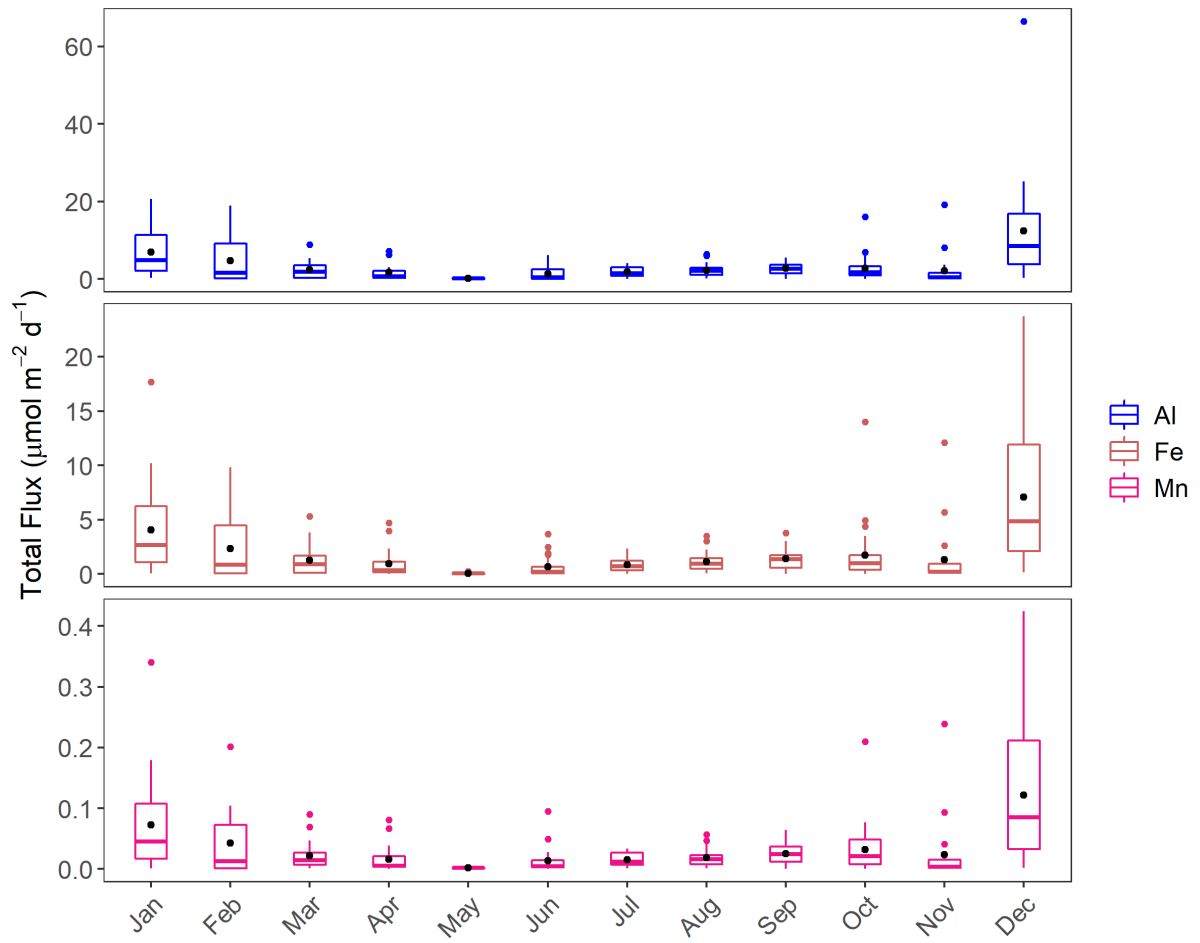


Figure 20. Boxplots of monthly deposition fluxes of total Al, Fe and Mn.

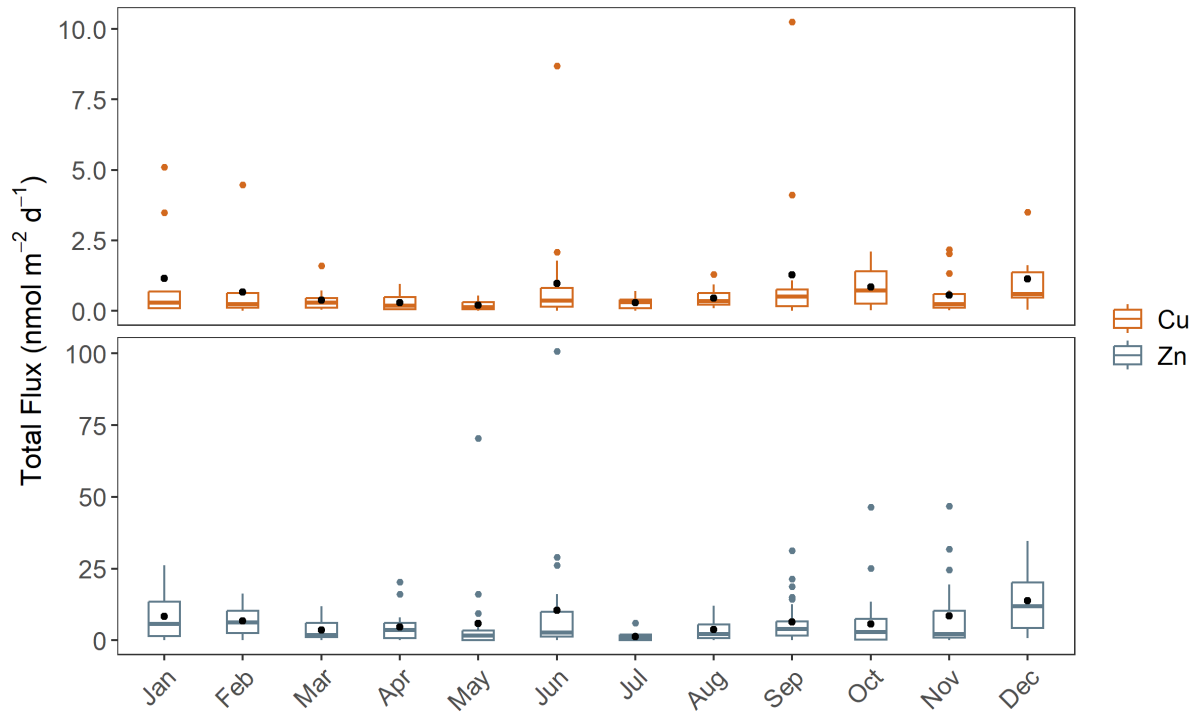


Figure 21. Boxplots of monthly deposition fluxes of total Cu and Zn.

Table 3. Mean (\pm standard deviation) and range (in parentheses) of seasonal flux of total bioactive trace metals and soluble major nutrients.

	Unit	Winter	Spring	Summer	Autumn
Al	$\mu\text{mol}/\text{m}^2/\text{d}$	8.13 ± 10.13 (0.03 - 66.52)	1.43 ± 2.08 (0.00 - 8.94)	1.79 ± 1.71 (0.00 - 6.37)	2.58 ± 3.09 (0.00 - 19.17)
Mn	$\mu\text{mol}/\text{m}^2/\text{d}$	0.08 ± 0.09 (0.0005 - 0.42)	0.01 ± 0.02 (0.0004 - 0.09)	0.02 ± 0.02 (0.00 - 0.10)	0.03 ± 0.04 (0.00 - 0.24)
Fe	$\mu\text{mol}/\text{m}^2/\text{d}$	4.58 ± 5.14 (0.02 - 23.71)	0.76 ± 1.21 (0.01 - 5.29)	0.86 ± 0.88 (0.00 - 3.67)	1.50 ± 2.23 (0.001 - 13.99)
V	$\text{nmol}/\text{m}^2/\text{d}$	10.21 ± 10.15 (0.26 - 50.31)	2.49 ± 2.86 (0.16 - 12.77)	3.43 ± 3.57 (0.37 - 25.42)	5.08 ± 5226.04 (0.29 - 38.45)
Zn	$\text{nmol}/\text{m}^2/\text{d}$	9.76 ± 8.92 (0.00 - 34.63)	4.73 ± 9.60 (0.00 - 70.50)	5.53 ± 13.42 (0.00 - 100.76)	6.70 ± 9.69 (0.00 - 46.77)
Cu	$\text{nmol}/\text{m}^2/\text{d}$	0.94 ± 1.46 (0.00 - 5.10)	0.28 ± 0.30 (0.00 - 1.59)	0.62 ± 1.34 (0.00 - 8.70)	$0.89 - 1.53$ (0.00 - 10.26)
Ni	$\text{nmol}/\text{m}^2/\text{d}$	2.85 ± 3.40 (0.15 - 10.50)	1.63 ± 2.69 (0.00 - 16.04)	3.57 ± 9.46 (0.00 - 48.94)	4.31 ± 13.45 (0.03 - 78.15)
NO_3^-	$\mu\text{mol}/\text{m}^2/\text{d}$	1.30 ± 0.56 (0.20 - 3.15)	1.10 ± 0.51 (0.27 - 2.61)	1.11 ± 9.46 (0.00 - 2.34)	1.30 ± 0.52 (0.26 - 2.66)
NH_4^+	$\mu\text{mol}/\text{m}^2/\text{d}$	0.07 ± 0.12 (0.00 - 0.65)	0.12 ± 0.10 (0.00 - 0.42)	0.12 ± 0.11 (0.00 - 0.58)	0.11 ± 0.12 (0.00 - 0.67)
PO_4^{3-}	$\text{nmol}/\text{m}^2/\text{d}$	1.76 ± 3.36 (0.00 - 19.88)	1.38 ± 2.90 (0.00 - 11.11)	2.14 ± 5.01 (0.00 - 38.65)	3.06 ± 3.90 (0.00 - 18.73)

From Fig. 22, the average monthly deposition fluxes of NO_3^- and NH_4^+ exhibited a bimodal pattern: with peaks for NO_3^- in March ($1.37 \pm 0.63 \mu\text{mol}/\text{m}^2/\text{d}$) and September ($1.47 \pm 0.48 \mu\text{mol}/\text{m}^2/\text{d}$) and for NH_4^+ , in May ($0.16 \pm 0.09 \mu\text{mol}/\text{m}^2/\text{d}$) and September ($0.15 \pm 0.12 \mu\text{mol}/\text{m}^2/\text{d}$). Additionally, for NO_3^- , the mean fluxes in the different seasons were comparable to one another (Table 3). For NH_4^+ , the lowest mean seasonal flux was observed in winter and the highest in summer (Table 3). For PO_4^{3-} , the maximum and minimum monthly mean fluxes were recorded in September ($0.004 \pm 0.004 \mu\text{mol}/\text{m}^2/\text{d}$) and May ($0.0004 \pm 0.0017 \mu\text{mol}/\text{m}^2/\text{d}$), respectively (Fig. 22). The season with the highest average flux of PO_4^{3-} was autumn. Overall, the average fluxes of the N species (NH_4^+ and NO_3^-) were approximately 10 and 100 times greater than the mean PO_4^{3-} fluxes, respectively.

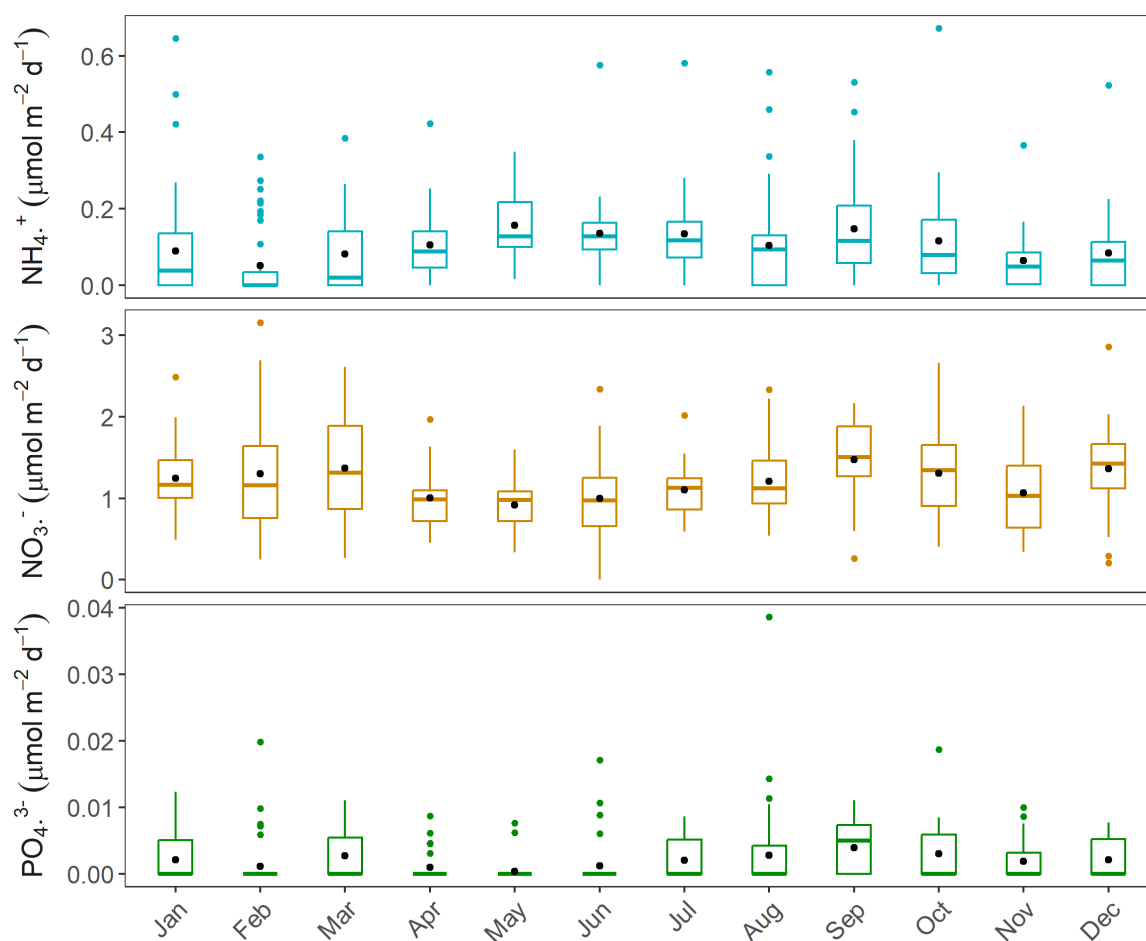


Figure 22. Boxplots of monthly deposition fluxes of NO_3^- , NH_4^+ and PO_4^{3-} .

The fluxes of NO_3^- showed a weak seasonal pattern, which implied that their sources were present throughout the seasons. Also, the monthly fluxes of NH_4^+ and NO_3^- exhibited an opposing pattern. Comparatively lower fluxes of NH_4^+ were matched by higher fluxes of NO_3^- in winter and vice versa in spring and summer. Chen et al. (2007) observed a similar behaviour in NH_4^+ and NO_3^- concentrations over the Gulf of Aqaba. They linked the observation to the prevalence of mineral dust with high NO_3^- content, and anthropogenic aerosols with high NH_4^+ content in winter and summer, respectively.

Seasonality in major regional sources of NH_4^+ (agriculture) and PO_4^{3-} (biomass burning) likely impacted variations in their seasonal deposition fluxes. Agriculture in West Africa relies heavily on rainfall (Sultan & Gaetani, 2016), with the dry season extending from November to February (Quagraine et al., 2020) and the wet season from May to October (Knippertz & Fink, 2008). The intensity of agricultural activities, and thus NH_3 emissions, are potentially minimal during the dry winter months: This could explain the estimated low mean NH_4^+ deposition flux in winter. In contrast, months of the summer rainfall (agriculture) season are associated with

higher monthly NH_4^+ fluxes. Also, in the Cape Verde region, the ocean is identified as a key source of NH_4^+ in spring (Fomba et al., 2014). Furthermore, the dry season coincides with the period of frequent biomass burning (forest fires, savannah fires, and burning to clear farmlands) in West Africa (Marufu et al., 2000). Consequently, emissions from biomass burning enriched transported particles with soluble P and influenced its seasonal flux. Hence, biomass burning and the prevalence of dust outbreaks during autumn and winter may account for the high PO_4^{3-} flux recorded for these seasons.

4.6 Redfield ratio

To provide a quantitative basis for exploring the possible impacts of atmospheric nutrient input on ocean biogeochemistry, the molar ratio of the N to P (Redfield ratio) in PM_{10} samples was estimated. The total P was PO_4^{3-} , while the total N was a combination of NO_3^- , NO_2^- , and NH_4^+ . From these estimates, a large temporal variation was observed. The average molar ratio of soluble inorganic N to P during the sampling period was ~ 251 . The seasonal ratios are ~ 256 , ~ 264 , ~ 223 , and ~ 260 for winter, spring, summer, and autumn, respectively. Figure 23 shows the seasonal variation in the calculated N:P ratios. Between the seasons, only summer had all three of its months recording ratios below the overall average of 251:1. The maximum and minimum N:P ratios were recorded in the spring months of March and May, respectively.

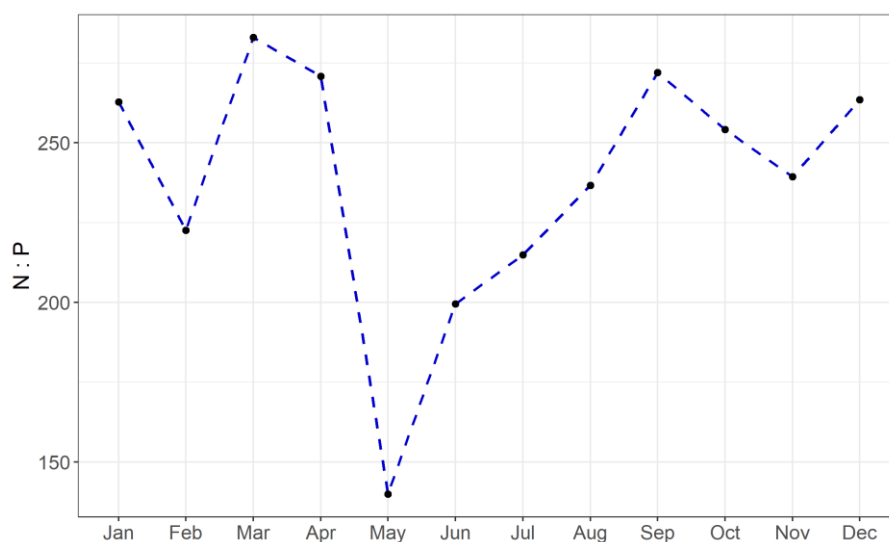


Figure 23. Monthly mean molar N:P ratio in aerosol samples.

The estimated ratios of N to P were found to far exceed the optimum value of 16:1, as stated by Moore et al. (2013). Among the various contributors to the total soluble inorganic N, NO_3^- dominated with fluxes of at least one order of magnitude greater. The fluxes of NO_3^- therefore

exerted more control on trends in total N and, consequently N:P ratios. This influence may have caused the similar pattern observed in the lowest monthly mean NO_3^- flux and N:P ratio occurring in May, as well as their bimodal peak values in March and September, as shown in Figs. 22 and 23. Typically, very high N:P ratios in the soluble fraction of atmospheric aerosols deposited in the North Atlantic Ocean have been reported (Chien et al., 2016; López-García et al., 2021; Powell et al., 2015; Zamora et al., 2013). The results here are therefore consistent with previous studies.

4.7 Implications of the study

Marine phytoplankton production is influenced by the balance between the levels of available N and P. The ideal stoichiometric N:P ratio, known as the Redfield ratio, is 16:1 (Moore et al., 2013). With this ratio as a benchmark, there is a hint that P availability is more critical to phytoplankton productivity compared to N (Mahowald et al., 2017). The results of this study indicated that aerosols deposited to the ETNA ocean were P-limited with respect to phytoplankton needs. Excess N from the high N:P ratio in atmospheric deposition may reduce N limitation but promote P limitation in the surface waters of the oligotrophic ETNA ocean. This argument is strengthened by the fact that other nutrient sources (such as upwelling) in the region are limited and have low N:P ratios (Chien et al., 2016). Thus, the ETNA Ocean is proposed to be a P-limited region. In contrast to other ocean basins, Krishnamurthy et al. (2010) expressed that in the North Atlantic, excess N usually accumulates in the thermocline: a region of sharp temperature change that separates the surface mixed layer from deep waters.

The high N:P ratio noted in atmospheric deposition can elicit varied responses in phytoplankton. In tropical waters, including the ETNA, autotrophic communities are dominated by picoplankton such as *Prochlorococcus*, *Synechococcus*, and picoeukaryotes (Dandonneau et al., 2004). These autotrophs have different cellular elemental stoichiometries, and thus differing vulnerabilities to nutrient limitation. Under P-limited, high N:P ratio conditions, *Prochlorococcus* is better equipped to survive at the expense of *Synechococcus* and picoeukaryotes, which have lower N:P quotas (Chien et al., 2016). The adaptive mechanisms of *Prochlorococcus* include a reduced demand for P, efficient P uptake and storage, and low use of P building blocks (Chien et al., 2016). *Prochlorococcus* prevalence can shift phytoplankton community structure and reduce carbon export to the ocean bottom, as particle sinking in small-cell-dominated environments is often slow (Chien et al., 2016).

Apart from atmospheric deposition, N₂ fixation by diazotrophs is another source of new N to the upper ocean. Diazotrophs rely on Fe availability to fix N₂ (Krishnamurthy et al., 2010; Marañón et al., 2010). In the ETNA, Fe is not limiting, as the region experiences high deposition of Fe-rich particles (Patey et al., 2015). In addition, while the solubility of the deposited trace elements in this area was not measured, dust Fe solubility is reported to be low (< 4 %; Mahowald et al., 2018). Upon particle deposition, this fraction is expected to have increased as the estimated total Fe flux in this study received contribution from anthropogenic emissions in addition to dust. Particle enrichment by anthropogenic emissions and atmospheric processing during long-range transport increases aerosol Fe solubility. Therefore, if Fe is bioavailable, N₂ fixation by diazotrophs should increase; however, this is likely not the case because diazotrophs are poor competitors for available Fe and P (Krishnamurthy et al., 2010). Diazotrophs have also been reported to be co-limited by P and Fe (Bristow et al., 2017). As a result, despite the presence of Fe, the P-limitation induced by atmospheric deposition in the ETNA reduces the contribution of new nitrogen from diazotrophs. This argument is further supported by modelling studies by Krishnamurthy et al. (2010), which indicated that increased N deposition to the ocean may be balanced by reduced N₂ fixation. Also, Herbert et al. (2018) expressed that the P-limited eastern Mediterranean region, with a high N:P deposition ratio, experiences low N₂ fixation.

Global warming is increasing sea surface temperature (SST), especially in open ocean areas (Siemer et al., 2021). Increasing SST enhances thermal stratification and limits vertical mixing, thus reducing nutrient input to the euphotic zone from deeper waters (Wrightson & Tagliabue, 2020). This scenario coupled with the shallow thermocline of the ETNA (Rugg et al., 2016), can enhance the influence of atmospheric deposition in controlling nutrient availability in the surface waters of the ETNA.

5. Conclusions

In this study, variations in PM₁₀ and associated nutrient fluxes over the Cabo Verde Islands in the ETNA were quantified. Potential sources of nutrient species were also identified. The PM₁₀ mass concentration exhibited a strong temporal and seasonal variation largely driven by atmospheric dynamics, with the influence of the Azores high and the SAL particularly pertinent. Similarly, the PM derived nutrient fluxes also showed strong temporal and seasonal variability. The aerosol particles reaching the CVAO were due to long-range transport. Consequently, different remote source regions were identified to contribute to particle loading and nutrient budgets over the island and surrounding oligotrophic open ocean. Continental source regions dominated this contribution in comparison to marine source areas. Overall, transported particles were impacted by arid desert areas, marine regions, and coastal and urban areas, which served as locations for anthropogenic aerosol emissions.

The aerosol sources that influenced atmospheric nutrients in the region were generally season-dependent. Dust outbreaks, prevalent in winter, drove seasonal variation in the flux of the bioactive elements Al, Fe and Mn. Emissions from regional biomass burning and agriculture likely contributed to the seasonality in PO₄³⁻ and NH₄⁺ fluxes, respectively.

Furthermore, estimated N:P ratios in the aerosol particles far exceeded the Redfield ratio of 16:1. Atmospheric nutrient deposition to the ETNA was thus P-limited in relation to phytoplankton needs. However, plankton (such as *Prochlorococcus*) adapted to P-limitation may thrive. Additionally, based on the high N:P ratio, the ETNA is proposed to be a P-limited region. This limitation may alter phytoplankton community structure, N₂ fixation rate, and subsequently change the biogeochemical cycles of N and C.

To gain a more comprehensive understanding of the implications of the results, particularly those related to nutrient deposition, this work can be supported by satellite remote sensing or in situ incubation experiments to evaluate the phytoplankton community that survives under such oligotrophic conditions. Future studies should use comparable long-term datasets to elucidate the variation in fluxes of the soluble trace nutrients. Moreover, investigating the specific anthropogenic activities supplying nutrients to the region could provide further insights into the relationship between policies against anthropogenic emissions and biological production in oligotrophic open ocean areas.

6. References

- Anderson, R. F., Cheng, H., Edwards, R. L., Fleisher, M. Q., Hayes, C. T., Huang, K. F., ... & Shelley, R. U. (2016). How well can we quantify dust deposition to the ocean? *Philosophical Transactions of the Royal Society A: Mathematical, Physical and Engineering Sciences*, 374(2081). <https://doi.org/10.1098/rsta.2015.0285>
- Ayanlade, A., Atai, G., & Jegede, M. O. (2019). Spatial and seasonal variations in atmospheric aerosols over Nigeria: Assessment of influence of intertropical discontinuity movement. *Journal of Ocean and Climate: Science, Technology and Impacts*, 9, 175931311882030. <https://doi.org/10.1177/1759313118820306>
- Baker, A. R., Adams, C., Bell, T. G., Jickells, T. D., & Ganzeveld, L. (2013). Estimation of atmospheric nutrient inputs to the Atlantic Ocean from 50°N to 50°S based on large-scale field sampling: Iron and other dust-associated elements. *Global Biogeochemical Cycles*, 27(3), 755–767. <https://doi.org/10.1002/gbc.20062>
- Baker, A. R., & Jickells, T. D. (2017). Atmospheric deposition of soluble trace elements along the Atlantic Meridional Transect (AMT). *Progress in Oceanography*, 158, 41–51. <https://doi.org/10.1016/j.pocean.2016.10.002>
- Baker, A. R., Weston, K., Kelly, S. D., Voss, M., Streu, P., & Cape, J. N. (2007). Dry and wet deposition of nutrients from the tropical Atlantic atmosphere: Links to primary productivity and nitrogen fixation. *Deep-Sea Research Part I: Oceanographic Research Papers*, 54(10), 1704–1720. <https://doi.org/10.1016/j.dsr.2007.07.001>
- Baker, A. R., Lesworth, T., Adams, C., Jickells, T. D., & Ganzeveld, L. (2010). Estimation of atmospheric nutrient inputs to the Atlantic ocean from 50°N to 50°S based on large-scale field sampling: Fixed nitrogen and dry deposition of phosphorus. *Global Biogeochemical Cycles*, 24(7), 1–16. <https://doi.org/10.1029/2009GB003634>
- Barkley, A. E., Prospero, J. M., Mahowald, N., Hamilton, D. S., Poppendorf, K. J., Oehlert, A. M., ... & Gaston, C. J. (2019). African biomass burning is a substantial source of phosphorus deposition to the Amazon, Tropical Atlantic Ocean, and Southern Ocean. *Proceedings of the National Academy of Sciences of the United States of America*, 116(33), 16216–16221. <https://doi.org/10.1073/pnas.1906091116>
- Berthold, M., Wulff, R., Reiff, V., Karsten, U., Nausch, G., & Schumann, R. (2019). Magnitude and influence of atmospheric phosphorus deposition on the southern Baltic Sea coast over

- 23 years: implications for coastal waters. *Environmental Sciences Europe*, 31(1).
<https://doi.org/10.1186/s12302-019-0208-y>
- Bristow, L. A., Mohr, W., Ahmerkamp, S., & Kuypers, M. M. M. (2017). Nutrients that limit growth in the ocean. *Current Biology*, 27(11), R474–R478.
<https://doi.org/10.1016/j.cub.2017.03.030>
- Bruker Nano GmbH. (2017). *Principles of TXRF Elemental Analysis with Total Reflection X-ray Fluorescence Spectrometry*. www.bruker.com
- Carpenter, L. J., Fleming, Z. L., Read, K. A., Lee, J. D., Moller, S. J., Hopkins, J. R., ... & Wallace, D. W. (2010). Seasonal characteristics of tropical marine boundary layer air measured at the cape verde atmospheric observatory. *Journal of Atmospheric Chemistry*, 67(2–3), 87–140. <https://doi.org/10.1007/s10874-011-9206-1>
- Castillo, S., Alastuey, A., Cuevas, E., Querol, X., & Avila, A. (2017). Quantifying dry and wet deposition fluxes in two regions of contrasting African influence: The NE Iberian Peninsula and the Canary Islands. *Atmosphere*, 8(5).
<https://doi.org/10.3390/atmos8050086>
- Chagué-Goff, C., & Wong, H. K. Y. (2013). 14.23 Wet Chemical Methods (pH, Electrical Conductivity, Ion-Selective Electrodes, Colorimetric Analysis, Ion Chromatography, Flame Atomic Absorption Spectrometry, Inductively Coupled Plasma-Atomic Emission Spectroscopy, and Quadrupole Inductively Coupled Plasma-Mass Spectrometry). *Treatise on Geomorphology*, 14, 274–281. <https://doi.org/10.1016/B978-0-12-374739-6.00391-2>
- Chen, H., Li, L., Lei, Y., Wu, S., Yan, D., & Dong, Z. (2020). Public health effect and its economics loss of PM_{2.5} pollution from coal consumption in China. *Science of the Total Environment*, 732. <https://doi.org/10.1016/j.scitotenv.2020.138973>
- Chen, Y., Mills, S., Street, J., Golan, D., Post, A., Jacobson, M., & Paytan, A. (2007). Estimates of atmospheric dry deposition and associated input of nutrients to Gulf of Aqaba seawater. *Journal of Geophysical Research Atmospheres*, 112(4).
<https://doi.org/10.1029/2006JD007858>
- Chien, C.-T., Mackey, K. R. M., Dutkiewicz, S., Mahowald, N. M., Prospero, J. M., & Paytan, A. (2016). Effects of African dust deposition on phytoplankton in the western tropical Atlantic Ocean off Barbados. *Global Biogeochemical Cycles*, 30(5), 716–734.
<https://doi.org/10.1002/2015GB005334>

- Dandonneau, Y., Deschamps, P. Y., Nicolas, J. M., Loisel, H., Blanchot, J., Montel, Y., ... & Bécu, G. (2004). Seasonal and interannual variability of ocean color and composition of phytoplankton communities in the North Atlantic, equatorial Pacific and South Pacific. *Deep-Sea Research Part II: Topical Studies in Oceanography*, 51(1–3), 303–318. <https://doi.org/10.1016/j.dsr2.2003.07.018>
- Deabji, N., Fomba, K. W., El Hajjaji, S., Mellouki, A., Poulain, L., Zeppenfeld, S., & Herrmann, H. (2021). First insights into northern Africa high-altitude background aerosol chemical composition and source influences. *Atmospheric Chemistry and Physics*, 21(24), 18147–18174. <https://doi.org/10.5194/acp-21-18147-2021>
- Desboeufs, K., Bon Nguyen, E., Chevaillier, S., Triquet, S., & Dulac, F. (2018). Fluxes and sources of nutrient and trace metal atmospheric deposition in the northwestern Mediterranean. *Atmospheric Chemistry and Physics*, 18(19), 14477–14492. <https://doi.org/10.5194/acp-18-14477-2018>
- Duce, R. A., Galloway, J. N., & Liss, P. S. (2009). The impacts of atmospheric deposition to the ocean on marine ecosystems and climate. *WMO Bulletin*, 58(1).
- Fomba, K. W., Deabji, N., Barcha, S. E. I., Ouchen, I., Elbaramoussi, E. M., El Moursli, R. C., ... & Herrmann, H. (2020). Application of TXRF in monitoring trace metals in particulate matter and cloud water. *Atmospheric Measurement Techniques*, 13(9), 4773–4790. <https://doi.org/10.5194/amt-13-4773-2020>
- Fomba, K. W., Müller, K., van Pinxteren, D., & Herrmann, H. (2013). Aerosol size-resolved trace metal composition in remote northern tropical atlantic marine environment: Case study cape verde islands. *Atmospheric Chemistry and Physics*, 13(9), 4801–4814. <https://doi.org/10.5194/acp-13-4801-2013>
- Fomba, K. W., Müller, K., van Pinxteren, D., Poulain, L., van Pinxteren, M., & Herrmann, H. (2014). Long-term chemical characterization of tropical and marine aerosols at the Cape Verde Atmospheric Observatory (CVAO) from 2007 to 2011. *Atmospheric Chemistry and Physics*, 14(17), 8883–8904. <https://doi.org/10.5194/acp-14-8883-2014>
- Fomba, K. W., Müller, K., Hofer, J., Makhmudov, A. N., Althausen, D., Nazarov, B. I., ... & Herrmann, H. (2019). Variations of the aerosol chemical composition during Asian dust storm at Dushanbe, Tajikistan. *E3S Web of Conferences*, 99. <https://doi.org/10.1051/E3SCONF/20199903007>

- Freire, S. M., Relvas, H., & Lopes, M. (2020). Impact of traffic emissions on air quality in Cabo Verde. *Environmental Monitoring and Assessment*, 192(11). <https://doi.org/10.1007/s10661-020-08690-8>
- Gama, C., Tchepel, O., Baldasano, J. M., Basart, S., Ferreira, J., Pio, C., ... & Borrego, C. (2015). Seasonal patterns of Saharan dust over Cape Verde—a combined approach using observations and modelling. *Tellus B: Chemical and Physical Meteorology*, 67(1). <https://doi.org/10.3402/tellusb.v67.24410>
- Gelado-Caballero, M. D., López-García, P., Prieto, S., Patey, M. D., Collado, C., & Hernández-Brito, J. J. (2012). Long-term aerosol measurements in Gran Canaria, Canary Islands: Particle concentration, sources and elemental composition. *Journal of Geophysical Research: Atmospheres*, 117(D03304).
- Ghan, S. J., Liu, X., Easter, R. C., Zaveri, R., Rasch, P. J., Yoon, J. H., & Eaton, B. (2012). Toward a minimal representation of aerosols in climate models: Comparative decomposition of aerosol direct, semidirect, and indirect radiative forcing. *Journal of Climate*, 25(19), 6461–6476. <https://doi.org/10.1175/JCLI-D-11-00650.1>
- Giechaskiel, B., Joshi, A., Ntziachristos, L., & Dilara, P. (2019). European regulatory framework and particulate matter emissions of gasoline light-duty vehicles: A review. *Catalysts*, 9(7). <https://doi.org/10.3390/catal9070586>
- Gong, X., Wex, H., Voigtländer, J., Fomba, K. W., Weinhold, K., van Pinxteren, M., ... & Stratmann, F. (2020). Characterization of aerosol particles at Cabo Verde close to sea level and at the cloud level—Part 1: Particle number size distribution, cloud condensation nuclei and their origins. *Atmospheric Chemistry and Physics*, 20(3), 1431-1449. <https://doi.org/10.5194/acp-20-1431-2020>
- Guo, C., Zhou, Y., Zhou, H., Su, C., & Kong, L. (2022). Aerosol Nutrients and Their Biological Influence on the Northwest Pacific Ocean (NWPO) and Its Marginal Seas. *Biology*, 11(6). <https://doi.org/10.3390/BIOLOGY11060842>
- Hamilton, D. S., Perron, M. M., Bond, T. C., Bowie, A. R., Buchholz, R. R., Guieu, C., ... & Mahowald, N. M. (2022). Earth, wind, fire, and pollution: Aerosol nutrient sources and impacts on ocean biogeochemistry. *Annual Review of Marine Science*, 14, 303-330. <https://doi.org/10.1146/annurev-marine-031921-013612>
- Herbert, R. J., Krom, M. D., Carslaw, K. S., Stockdale, A., Mortimer, R. J. G., Benning, L. G.,

- ... & Browse, J. (2018). The effect of atmospheric acid processing on the global deposition of bioavailable phosphorus from dust. *Global Biogeochemical Cycles*, 32(9), 1367-1385. <https://doi.org/10.1029/2018GB005880>
- Hickman, J. E., Andela, N., Dammers, E., Clarisse, L., Coheur, P. F., Van Damme, M., ... & Bauer, S. E. (2021). Changes in biomass burning, wetland extent, or agriculture drive atmospheric NH₃ trends in select African regions. *Atmospheric Chemistry and Physics*, 21(21), 16277-16291. <https://doi.org/10.5194/acp-21-16277-2021>
- Jickells, T. D., Baker, A. R., & Chance, R. (2016). Atmospheric transport of trace elements and nutrients to the oceans. *Philosophical Transactions of the Royal Society A: Mathematical, Physical and Engineering Sciences*, 374(2081). <https://doi.org/10.1098/rsta.2015.0286>
- Jin, X., Zhu, Q., & Cohen, R. C. (2021). Direct estimates of biomass burning NO_x emissions and lifetimes using daily observations from TROPOMI. *Atmospheric Chemistry and Physics*, 21(20), 15569–15587. <https://doi.org/10.5194/acp-21-15569-2021>
- Johansen, A. M., Siefert, R. L., & Hoffmann, M. R. (2000). Chemical composition of aerosols collected over the tropical North Atlantic Ocean. *Journal of Geophysical Research Atmospheres*, 105(D12), 15277–15312. <https://doi.org/10.1029/2000JD900024>
- Jordi, A., Basterretxea, G., Tovar-Sánchez, A., Alastuey, A., & Querol, X. (2012). Copper aerosols inhibit phytoplankton growth in the Mediterranean Sea. *Proceedings of the National Academy of Sciences*, 109(52), 21246-21249. <https://doi.org/10.1073/PNAS.1207567110>
- Kanakidou, M., Myriokefalitakis, S., & Tsigaridis, K. (2018). Aerosols in atmospheric chemistry and biogeochemical cycles of nutrients. *Environmental Research Letters*, 13(6). <https://doi.org/10.1088/1748-9326/aabcbd>
- Kaufman, Y. J., Tanré, D., & Boucher, O. (2002). A satellite view of aerosols in the climate system. *Nature*, 419(6903), 215–223. <https://doi.org/10.1038/nature01091>
- Kaushik, A., Kumar, A., Aswini, M. A., Panda, P. P., Shukla, G., & Gupta, N. C. (2021). Seasonal Variation in Chemical Composition of Size-Segregated Aerosols Over the Northeastern Arabian Sea. *Frontiers in Environmental Science*, 8, 1–18. <https://doi.org/10.3389/fenvs.2020.619174>
- Kelly, F. J., & Fussell, J. C. (2012). Size, source and chemical composition as determinants of toxicity attributable to ambient particulate matter. *Atmospheric Environment*, 60, 504–

526. <https://doi.org/10.1016/j.atmosenv.2012.06.039>

- Kiko, R., Brandt, P., Christiansen, S., Faustmann, J., Kriest, I., Rodrigues, E., ... & Hauss, H. (2020). Zooplankton-mediated fluxes in the eastern tropical North Atlantic. *Frontiers in Marine Science*, 7. <https://doi.org/10.3389/fmars.2020.00358>
- Klimont, Z., Kupiainen, K., Heyes, C., Purohit, P., Cofala, J., Rafaj, P., ... & Schöpp, W. (2017). Global anthropogenic emissions of particulate matter including black carbon. *Atmospheric Chemistry and Physics*, 17(14), 8681-8723. <https://doi.org/10.5194/acp-17-8681-2017>
- Knippertz, P., & Fink, A. H. (2008). Dry-season precipitation in tropical West Africa and its relation to forcing from the extratropics. *Monthly Weather Review*, 136(9), 3579–3596. <https://doi.org/10.1175/2008MWR2295.1>
- Kolb, C. E., & Worsnop, D. R. (2012). Chemistry and composition of atmospheric aerosol particles. *Annual Review of Physical Chemistry*, 63, 471–491. <https://doi.org/10.1146/annurev-physchem-032511-143706>
- Krishnamurthy, A., Moore, J. K., Mahowald, N. M., Luo, C., & Zender, C. S. (2010). Impacts of atmospheric nutrient inputs on marine biogeochemistry. *Journal of Geophysical Research*, 115(G1). <https://doi.org/10.1029/2009jg001115>
- Kumar, A., Abouchami, W., Galer, S. J. G., Singh, S. P., Fomba, K. W., Prospero, J. M., & Andreae, M. O. (2018). Seasonal radiogenic isotopic variability of the African dust outflow to the tropical Atlantic Ocean and across to the Caribbean. *Earth and Planetary Science Letters*, 487, 94–105. <https://doi.org/10.1016/j.epsl.2018.01.025>
- Kumari, S., Jain, M. K., & Elumalai, S. P. (2021). Assessment of pollution and health risks of heavy metals in particulate matter and road dust along the road network of Dhanbad, India. *Journal of Health and Pollution*, 11(29). <https://doi.org/10.5696/2156-9614-11.29.210305>.
- López-García, P., Gelado-Caballero, M. D., Patey, M. D., & Hernández-Brito, J. J. (2021). Atmospheric fluxes of soluble nutrients and Fe: More than three years of wet and dry deposition measurements at Gran Canaria (Canary Islands). *Atmospheric Environment*, 246. <https://doi.org/10.1016/j.atmosenv.2020.118090>
- Mahowald, N. (2011). Aerosol indirect effect on biogeochemical cycles and climate. *Science*, 334(6057), 794-796. <https://doi.org/10.1126/science.1207374>
- Mahowald, N. M., Hamilton, D. S., Mackey, K. R. M., Moore, J. K., Baker, A. R., Scanza, R.

- A., & Zhang, Y. (2018). Aerosol trace metal leaching and impacts on marine microorganisms. *Nature Communications*, 9(1). <https://doi.org/10.1038/s41467-018-04970-7>
- Mahowald, N. M., Scanza, R., Brahney, J., Goodale, C. L., Hess, P. G., Moore, J. K., & Neff, J. (2017). Aerosol deposition impacts on land and ocean carbon cycles. *Current Climate Change Reports*, 3, 16-31. <https://doi.org/10.1007/s40641-017-0056-z>
- Mahowald, N. M., Ward, D. S., Kloster, S., Flanner, M. G., Heald, C. L., Heavens, N. G., Hess, P. G., Lamarque, J. F., & Chuang, P. Y. (2011). Aerosol impacts on climate and biogeochemistry. *Annual Review of Environment and Resources*, 36, 45–74. <https://doi.org/10.1146/annurev-environ-042009-094507>
- Marañón, E., Fernández, A., Mouriño-Carballido, B., Martínez-García, S., Teira, E., Cermeño, P.,... & Achterberg, E. P. (2010). Degree of oligotrophy controls the response of microbial plankton to Saharan dust. *Limnology and Oceanography*, 55(6), 2339-2352. <https://doi.org/10.4319/LO.2010.55.6.2339>
- Mateus-Fontecha, L., Vargas-Burbano, A., Jimenez, R., Rojas, N. Y., Rueda-Saa, G., van Pinxteren, D., ... & Herrmann, H. (2022). Understanding aerosol composition in a tropical inter-Andean valley impacted by agro-industrial and urban emissions. *Atmospheric Chemistry and Physics*, 22(13), 8473-8495. <https://doi.org/10.5194/acp-22-8473-2022>
- Moore, C. M., Mills, M. M., Arrigo, K. R., Berman-Frank, I., Bopp, L., Boyd, P. W., ... & Ulloa, O. (2013). Processes and patterns of oceanic nutrient limitation. *Nature geoscience*, 6(9), 701-710. <https://doi.org/10.1038/ngeo1765>
- Myriokefalitakis, S., Ito, A., Kanakidou, M., Nenes, A., Krol, M. C., Mahowald, N. M., ... & Duce, R. A. (2018). Reviews and syntheses: the GESAMP atmospheric iron deposition model intercomparison study. *Biogeosciences*, 15(21), 6659-6684. <https://doi.org/10.5194/bg-15-6659-2018>
- Niedermeier, N., Held, A., Müller, T., Heinold, B., Schepanski, K., Tegen, I., ... & Wiedensohler, A. (2014). Mass deposition fluxes of Saharan mineral dust to the tropical northeast Atlantic Ocean: an intercomparison of methods. *Atmospheric Chemistry and Physics*, 14(5), 2245-2266. <https://doi.org/10.5194/acp-14-2245-2014>
- O'Dowd, C., Ceburnis, D., Ovadnevaite, J., Rinaldi, M., & Facchini, M. . (2013). Do anthropogenic or coastal aerosol sources impact on a clean marine aerosol signature at

- Mace Head? *Atmospheric Chemistry and Physics Discussions*, 13(3), 7311–7347.
<https://doi.org/10.5194/acpd-13-7311-2013>
- Okin, G. S., Baker, A. R., Tegen, I., Mahowald, N. M., Dentener, F. J., Duce, R. A., ... & Zhu, T. (2011). Impacts of atmospheric nutrient deposition on marine productivity: Roles of nitrogen, phosphorus, and iron. *Global Biogeochemical Cycles*, 25(2), 1–10.
<https://doi.org/10.1029/2010GB003858>
- Patey, M. D., Achterberg, E. P., Rijkenberg, M. J., & Pearce, R. (2015). Aerosol time-series measurements over the tropical Northeast Atlantic Ocean: Dust sources, elemental composition and mineralogy. *Marine Chemistry*, 174, 103–119.
<https://doi.org/10.1016/j.marchem.2015.06.004>
- Paulot, F., Jacob, D. J., Johnson, M. T., Bell, T. G., Baker, A. R., Keene, W. C., ... & Stock, C. A. (2015). Global oceanic emission of ammonia: Constraints from seawater and atmospheric observations. *Global Biogeochemical Cycles*, 29(8), 1165–1178.
<https://doi.org/10.1002/2015GB005106>
- Paytan, A., Mackey, K. R., Chen, Y., Lima, I. D., Doney, S. C., Mahowald, N., ... & Post, A. F. (2009). Toxicity of atmospheric aerosols on marine phytoplankton. *Proceedings of the National Academy of Sciences*, 106(12), 4601–4605.
<https://doi.org/10.1073/PNAS.0811486106>
- Pinedo-González, P., West, A. J., Tovar-Sánchez, A., Duarte, C. M., Marañón, E., Cermeño, P., ... & Sañudo-Wilhelmy, S. A. (2015). Surface distribution of dissolved trace metals in the oligotrophic ocean and their influence on phytoplankton biomass and productivity. *Global Biogeochemical Cycles*, 29(10), 1763–1781.
<https://doi.org/10.1002/2015GB005149>
- Powell, C. F., Baker, A. R., Jickells, T. D., W. Bange, H., Chance, R. J., & Yodanis, C. (2015). Estimation of the atmospheric flux of nutrients and trace metals to the eastern tropical North Atlantic Ocean. *Journal of the Atmospheric Sciences*, 72(10), 4029–4045.
<https://doi.org/10.1175/JAS-D-15-0011.1>
- Prather, K. A., Hatch, C. D., & Grassian, V. H. (2008). Analysis of atmospheric aerosols. *Annual Review of Analytical Chemistry*, 1(1), 485–514.
<https://doi.org/10.1146/annurev.anchem.1.031207.113030>
- Priyadharshini, B., Verma, S., Chatterjee, A., Sharma, S. K., & Mandal, T. K. (2019). Chemical

- characterization of fine atmospheric particles of water-soluble ions and carbonaceous species in a tropical urban atmosphere over the eastern Indo-Gangetic plain. *Aerosol and Air Quality Research*, 19(1), 129–147. <https://doi.org/10.4209/aaqr.2017.12.0606>
- Qian, Y., Leung, L. R., Ghan, S. J., & Giorgi, F. (2011). Regional climate effects of aerosols over China: modeling and observation. *Tellus B: Chemical and Physical Meteorology*, 55(4), 914–934. <https://doi.org/10.3402/tellusb.v55i4.16379>
- Quagraine, K. A., Nkrumah, F., Klein, C., Klutse, N. A. B., & Quagraine, K. T. (2020). West African summer monsoon precipitation variability as represented by reanalysis datasets. *Climate*, 8(10), 1–18. <https://doi.org/10.3390/cli8100111>
- Rodríguez, S., & López-Darias, J. (2021). Dust and tropical PM_x aerosols in Cape Verde: Sources, vertical distributions and stratified transport from North Africa. *Atmospheric Research*, 263. <https://doi.org/10.1016/j.atmosres.2021.105793>
- Rugg, A., Foltz, G. R., & Perez, R. C. (2016). Role of mixed layer dynamics in tropical North Atlantic interannual sea surface temperature variability. *Journal of Climate*, 29(22), 8083–8101. <https://doi.org/10.1175/JCLI-D-15-0867.1>
- Schepanski, K., Tegen, I., & Macke, A. (2009). Saharan dust transport and deposition towards the tropical northern Atlantic. *Atmospheric Chemistry and Physics*, 9(4), 1173–1189. <https://doi.org/10.5194/acp-9-1173-2009>
- Seok, M. W., Kim, D., Park, G. H., Lee, K., Kim, T. H., Jung, J., ... & Kim, T. W. (2021). Atmospheric deposition of inorganic nutrients to the Western North Pacific Ocean. *Science of the Total Environment*, 793. <https://doi.org/10.1016/J.SCITOTENV.2021.148401>
- Siemer, J. P., Machín, F., González-Vega, A., Arrieta, J. M., Gutiérrez-Guerra, M. A., Pérez-Hernández, M. D., ... & Fraile-Nuez, E. (2021). Recent Trends in SST, Chl-a, Productivity and Wind Stress in Upwelling and Open Ocean Areas in the Upper Eastern North Atlantic Subtropical Gyre. *Journal of Geophysical Research: Oceans*, 126(8), e2021JC017268. <https://doi.org/10.1029/2021JC017268>
- Song, J., Zhao, Y., Zhang, Y., Fu, P., Zheng, L., Yuan, Q., ... & Lai, S. (2018). Influence of biomass burning on atmospheric aerosols over the western South China Sea: Insights from ions, carbonaceous fractions and stable carbon isotope ratios. *Environmental Pollution*, 242, 1800–1809. <https://doi.org/10.1016/j.envpol.2018.07.088>

- Stein, A. F., Draxler, R. R., Rolph, G. D., Stunder, B. J. B., Cohen, M. D., & Ngan, F. (2015). NOAA's HYSPLIT atmospheric transport and dispersion modeling system. *Bulletin of the American Meteorological Society*, *96*(12), 2059–2077. <https://doi.org/10.1175/BAMS-D-14-00110.1>
- Sudheer, A. K., & Rengarajan, R. (2012). Atmospheric mineral dust and trace metals over urban environment in western India during winter. *Aerosol and Air Quality Research*, *12*(5), 923–933. <https://doi.org/10.4209/aaqr.2011.12.0237>
- Sultan, B., & Gaetani, M. (2016). Agriculture in West Africa in the twenty-first century: climate change and impacts scenarios, and potential for adaptation. *Frontiers in plant science*, *7*, 1–20. <https://doi.org/10.3389/fpls.2016.01262>
- Sunda, W. G. (2012). Feedback interactions between trace metal nutrients and phytoplankton in the ocean. *Frontiers in Microbiology*, *3*. <https://doi.org/10.3389/fmicb.2012.00204>
- Tipping, E., Benham, S., Boyle, J. F., Crow, P., Davies, J., Fischer, U., ... & Toberman, H. (2014). Atmospheric deposition of phosphorus to land and freshwater. *Environmental Science: Processes & Impacts*, *16*(7), 1608-1617. <https://doi.org/10.1039/c3em00641g>
- Tomasi, C., & Lupi, A. (2016). Primary and Secondary Sources of Atmospheric Aerosol. *Atmospheric Aerosols*, 1–86. <https://doi.org/10.1002/9783527336449.ch1>
- Trapp, J. M., Millero, F. J., & Prospero, J. M. (2010). Trends in the solubility of iron in dust-dominated aerosols in the equatorial Atlantic trade winds: Importance of iron speciation and sources. *Geochemistry, Geophysics, Geosystems*, *11*(3). <https://doi.org/10.1029/2009GC002651>
- Van der Jagt, H., Friese, C., Stuut, J. B. W., Fischer, G., & Iversen, M. H. (2018). The ballasting effect of Saharan dust deposition on aggregate dynamics and carbon export: Aggregation, settling, and scavenging potential of marine snow. *Limnology and Oceanography*, *63*(3), 1386-1394. <https://doi.org/10.1002/LNO.10779>
- van Pinxteren, D., Brüggemann, E., Gnauk, T., Müller, K., Thiel, C., & Herrmann, H. (2010). A GIS based approach to back trajectory analysis for the source apportionment of aerosol constituents and its first application. *Journal of Atmospheric Chemistry*, *67*(1), 1–28. <https://doi.org/10.1007/s10874-011-9199-9>
- van Pinxteren, M., Fomba, K. W., Triesch, N., Stolle, C., Wurl, O., Bahlmann, E., ... & Herrmann, H. (2020). Marine organic matter in the remote environment of the Cape Verde

- islands—an introduction and overview to the MarParCloud campaign. *Atmospheric Chemistry and Physics*, 20(11), 6921-6951. <https://doi.org/10.5194/acp-20-6921-2020>
- Ventura, A., Simões, E. F. C., Almeida, A. S., Martins, R., Duarte, A. C., Loureiro, S., & Duarte, R. M. B. O. (2021). Deposition of aerosols onto upper ocean and their impacts on marine biota. *Atmosphere*, 12(6), 1–18. <https://doi.org/10.3390/atmos12060684>
- World Health Organization. (2013). Health Effects of Particulate Matter: Policy implications for countries in eastern Europe, Caucasus and central Asia. https://doi.org/10.1007/978-1-4615-4569-9_10
- Wrightson, L., & Tagliabue, A. (2020). Quantifying the Impact of Climate Change on Marine Diazotrophy: Insights From Earth System Models. *Frontiers in Marine Science*, 7, 1–9. <https://doi.org/10.3389/fmars.2020.00635>
- Zhong, Y., Wang, X., & Cheng, S. (2020). Characteristics and source apportionment of PM_{2.5} and O₃ during winter of 2013 and 2018 in Beijing. *Atmosphere*, 11(12). <https://doi.org/10.3390/atmos11121324>
- Zhou, L., Liu, F., Liu, Q., Fortin, C., Tan, Y., Huang, L., & Campbell, P. G. C. (2021). Aluminum increases net carbon fixation by marine diatoms and decreases their decomposition: Evidence for the iron–aluminum hypothesis. *Limnology and Oceanography*, 66(7), 2712–2727. <https://doi.org/10.1002/lno.11784>
- Zong, Z., Wang, X., Tian, C., Chen, Y., Fu, S., Qu, L., ... & Zhang, G. (2018). PMF and PSCF based source apportionment of PM_{2.5} at a regional background site in North China. *Atmospheric research*, 203, 207-215. <https://doi.org/10.1016/j.atmosres.2017.12.013>
- Zong, Z., Wang, X., Tian, C., Chen, Y., Qu, L., Ji, L., ... & Zhang, G. (2016). Source apportionment of PM_{2.5} at a regional background site in North China using PMF linked with radiocarbon analysis: insight into the contribution of biomass burning. *Atmospheric Chemistry and Physics*, 16(17), 11249-11265. <https://doi.org/10.5194/acp-16-11249-2016>

Appendices

Appendix A. Statistical summary of the mass concentration of particulate matter (PM₁₀), water soluble ions and trace metals analysed in the aerosol samples.

	Unit	Minimum	Maximum	Mean	SD
PM ₁₀ mass	µg/m ³	8.57	547.94	51.87	57.56
Cl ⁻	µg/m ³	0.79	16.74	5.87	2.46
NO ₃ ⁻	µg/m ³	0.00	2.41	1.11	0.47
SO ₄ ²⁻	µg/m ³	0.00	7.68	2.36	1.10
C ₂ O ₄ ²⁻	µg/m ³	0.00	0.51	0.10	0.06
NO ₂ ⁻	ng/m ³	0.00	10.23	0.16	0.71
Br ⁻	µg/m ³	0.00	0.08	0.00	0.01
F ⁻	ng/m ³	0.00	11.25	0.98	1.57
HCO ₂ ⁻	µg/m ³	0.00	0.11	0.01	0.01
MSA	µg/m ³	0.00	0.20	0.03	0.02
PO ₄ ³	ng/m ³	0.00	61.31	3.09	5.85
Na ⁺	µg/m ³	0.32	8.73	3.71	1.36
NH ₄ ⁺	µg/m ³	0.00	0.18	0.03	0.03
K ⁺	µg/m ³	0.00	0.53	0.17	0.08
Mg ²⁺	µg/m ³	0.00	2.19	0.45	0.19
Ca ²⁺	µg/m ³	0.00	4.44	0.77	0.73
Na	µg/m ³	5.44	248.60	25.15	24.30
Mg	µg/m ³	0.00	2.99	0.44	0.40
Al	µg/m ³	0.00	29.08	1.38	2.54
P	µg/m ³	0.00	2.37	0.04	0.16
S	µg/m ³	0.03	10.75	0.90	0.76
Cl	µg/m ³	0.00	1.73	0.07	0.13
Ar	µg/m ³	0.00	5.73	0.13	0.37
K	µg/m ³	0.00	12.16	0.71	1.15
Ca	µg/m ³	0.00	12.46	1.50	2.06
Sc	ng/m ³	0.68	18.89	4.89	7.83
Ti	µg/m ³	0.00	2.51	0.06	0.17
V	ng/m ³	0.11	44.79	4.03	5.60

Cr	µg/m ³	0.00	0.11	0.00	0.01
Mn	µg/m ³	0.00	0.41	0.03	0.05
Fe	µg/m ³	0.00	23.18	1.58	2.81
Ni	ng/m ³	0.00	62.83	2.65	7.52
Cu	ng/m ³	0.00	8.88	0.61	1.14
Zn	ng/m ³	0.00	104.45	6.47	10.67
As	ng/m ³	0.02	1.54	0.26	0.26
Se	ng/m ³	0.01	5.14	0.52	0.41
Br	ng/m ³	0.00	10.45	0.65	0.91
Rb	ng/m ³	0.00	31.89	2.03	3.71
Sr	µg/m ³	0.00	0.15	0.01	0.02
Y	ng/m ³	0.00	60.86	0.90	4.14
Zr	µg/m ³	0.00	0.47	0.06	0.05
Nb	µg/m ³	0.00	0.24	0.14	0.08
Mo	µg/m ³	0.00	0.77	0.39	0.55
Ru	µg/m ³	0.00	0.22	0.11	0.15
Rh	µg/m ³	0.00	1.48	0.02	0.12
Pd	µg/m ³	0.00	0.12	0.03	0.02
Ag	µg/m ³	0.00	5.07	0.06	0.32
In	µg/m ³	0.00	0.32	0.03	0.05
Sn	ng/m ³	1.25	19.41	11.14	9.19
Sb	ng/m ³	0.38	40.71	20.54	28.52
I	ng/m ³	0.00	4.06	1.85	1.84
Cs	ng/m ³	0.48	14.18	2.75	4.10
Ba	µg/m ³	0.00	0.33	0.02	0.04
La	ng/m ³	0.00	80.49	6.11	13.62
Ce	ng/m ³	0.00	10.69	0.56	1.80
Pr	ng/m ³	0.21	70.76	3.69	7.69
Nd	ng/m ³	0.08	46.17	3.19	6.21
Sm	ng/m ³	0.09	24.31	1.99	4.11
Eu	ng/m ³	0.00	4.89	0.38	1.21
Gd	ng/m ³	0.00	0.32	0.13	0.14
Tb	µg/m ³	0.00	0.28	0.06	0.06

Ho	ng/m ³	0.05	24.70	1.78	3.05
Er	ng/m ³	0.00	3.79	1.76	1.91
Yb	ng/m ³	0.00	16.87	1.12	2.13
Lu	ng/m ³	0.00	3.76	0.98	0.93
Hf	ng/m ³	0.07	6.10	1.54	2.27
W	ng/m ³	0.04	1.55	0.79	1.07
Ir	μg/m ³	0.00	0.44	0.02	0.06
Hg	ng/m ³	0.01	4.34	0.79	0.75
Tl	ng/m ³	0.96	2.26	1.61	0.92
Pb	ng/m ³	0.00	112.79	1.49	9.68
Bi	ng/m ³	0.06	0.68	0.27	0.28
Th	ng/m ³	0.00	1.58	0.15	0.21
U	ng/m ³	0.00	1.66	0.10	0.34

